

No part of this digital document may be reproduced, stored in a retrieval system or transmitted commercially in any form or by any means. The publisher has taken reasonable care in the preparation of this digital document, but makes no expressed or implied warranty of any kind and assumes no responsibility for any errors or omissions. No liability is assumed for incidental or consequential damages in connection with or arising out of information contained herein. This digital document is sold with the clear understanding that the publisher is not engaged in rendering legal, medical or any other professional services.

Chapter 4

FORCE-FEEDBACK HIGH-SPEED ATOMIC FORCE MICROSCOPE

Byung I. Kim and Ryan D. Boehm*

Boise State University, Department of Physics, Boise, ID, US

ABSTRACT

High-speed atomic force microscopy (HSAFM) has enabled researchers to view the nanometer-scale dynamic behavior of individual biological and bio-relevant molecules at a molecular-level resolution under physiologically relevant time scales, which is the realization of a dream in life sciences. These high-speed imaging applications now extend to the cellular/bacterial systems with the use of a smaller cantilever. By reducing the sizes of the HSAFM cantilevers by a factor of ten, systems have demonstrated image speeds up to 0.1 frames per second for larger biological systems such as bacteria. However, this imaging speed is insufficient to understand many rapid large-scale biological phenomena.

In this chapter, a newly developed novel HSAFM using force-feedback is introduced and discussed. This HSAFM is based on a newly developed force microscope called cantilever-based optical interfacial force microscope (COIFM). The COIFM system was originally developed to avoid snap-to-contact problem associated with conventional AFM in measuring normal and frictional forces as a function of distance between a probe and a sample. The HSAFM has been recently applied to the high-speed imaging of biological structures and to the mechanical property imaging of soft sample surfaces. This system has demonstrated topographic imaging capabilities with the imaging of *Escherichia coli* biofilm and planktonic cell structures. It also has the capacity to investigate the mechanical properties of soft materials while still avoiding the double-spring effect. The force-feedback HSAFM was shown to be stable for various speeds up to 5 frames per second in imaging softer adhesive biological samples. The system still uses a conventional-size self-actuation cantilever rather than using a smaller cantilever, thus avoiding arduous fabrication and signal detection with a smaller laser spot size associated with the use of a smaller cantilever. This novel force-feedback HSAFM will contribute greatly to the studies of large-scale biological phenomena.

* ¹To whom correspondence should be addressed. Email: ByungKim@boisestate.edu.

1. INTRODUCTION

The recent advancement of high-speed atomic force microscopy (HSAFM) has enabled researchers to view the nanometer-scale dynamic behavior of individual biological and bio-relevant molecules at a molecular-level resolution under physiologically relevant time scales [1-3] which is the realization of a dream in the life sciences. Such studies include the visualization of various dynamic activities carried out by biological macromolecules [4, 5], such as motor proteins and cytoskeletal fibers [1], nucleic acids/proteins in real time [2], and biopolymers [3, 6]. The enhancement of the scan speed, development of a high z-bandwidth feedback loop, and the advancement of tapping-mode imaging with a small cantilever make it possible to improve the resolution of topographic signals in both time and space in less invasive ways [1-5, 7-10].

These high-speed imaging applications now extend to the cellular/bacterial systems with the use of a smaller cantilever [11, 12]. The use of a small cantilever is based on the view that the limitation of imaging speed originates from the size of the cantilever, as the cantilever response speed is proportional to the cantilever resonance frequencies [6, 11]. The use of a cantilever with high-resonant vibrational frequency allows more rapid vertical tip movement, thus obtaining high-speed imaging. This has been accomplished by reducing the size of the cantilevers of HSAFM to a width of 10 μm and a length of 20-30 μm [11], instead of using conventional cantilevers that are tens of μm wide and hundreds of μm long. The systems have demonstrated image speeds up to 1 frame per second for small biomolecular structures, such as DNA, and 0.1 frames per second for larger biological systems, such as bacteria [6, 11, 12]. However, this imaging speed is insufficient to understand many rapid large-scale biological phenomena. For instance, the roughening variation of bacteria occurs within a few seconds in response to an antimicrobial [11, 13]. Also, the use of smaller cantilevers creates some challenges, such as fabrication and signal detection with a smaller laser spot size [1, 14].

In this chapter, a newly developed novel HSAFM using force-feedback is introduced and discussed. Instead of employing a small cantilever for high-speed imaging, the HSAFM is based on a newly developed force microscope called cantilever-based optical interfacial force microscope (COIFM) [15-17]. The COIFM was originally developed as an experimental technique to remove the rapid snap-to-contact problem associated with conventional AFM measurements [18-21].

The COIFM uses force-feedback to measure normal and frictional forces as a function of distance between a probe and a sample to understand fundamental interfacial interactions at nanometer scales. It has proven its ability to simultaneously measure normal and friction forces between two surfaces at the nanometer scale in ambient environments using lateral modulation [16, 17]. The force-feedback shortens the response time of the sensor, which is the most essential component of this HSAFM. Since the force-feedback HSAFM still uses a conventional-size self-actuation cantilever rather than using a smaller cantilever, it has a displacement capability of micrometers, thus enabling the system to extend to applications ranging from biomolecules to cellular systems. This system has demonstrated topographic imaging capabilities with the imaging of *Escherichia coli* biofilm and planktonic cell structures [22].

The HSAFM also has the capacity to investigate the mechanical properties of soft materials while still avoiding the double-spring effect (see Figure 1(a)). The HSAFM system

is able to make the spring constant of the cantilever (k_{cb}) infinite, in that the cantilever does not experience any deflection due to the applied counteractive force through the force-feedback mechanism, resulting in the zero-compliance of the cantilever or infinite cantilever spring constant [24]. Due to this zero-compliance of the cantilever, the only observed spring constant results from the adsorbed material (see Figure 1(b)). Based on this concept, the HSAFM is applied to acquire topographic structures and material properties simultaneously in the same area. The simultaneous acquisition is important to scientific understanding of various soft materials ranging from thin organic films to biomolecules [25] and for future applications, such as the development of micromechanical machines [26]. Finally, the applied loading force, hydrophilicity, and imaging rate influence on imaging stability of the force-feedback HSAFM. In particular, the force-feedback HSAFM is stable for various speeds up to 5 frames per second in imaging softer adhesive biological samples [27]. This novel force-feedback HSAFM has the potential to greatly contribute to the studies of these large-scale biological phenomena through the improvement of the time resolution for extensive scan sizes up to several micrometers [11-13]. The system still uses a conventional-size self-actuation cantilever rather than using a smaller cantilever, thus avoiding arduous fabrication and signal detection with a smaller laser spot size associated with the use of a smaller cantilever.

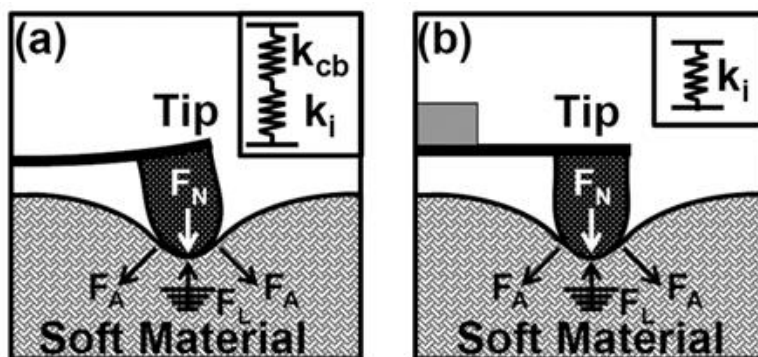


Figure 1. Schematic diagram of the viscoelasticity measurement using (a) an AFM and (b) a COIFM. As the tip presses down upon the soft material, adhesive capillary forces (F_A) from the sample and the depression forces from the spring constant of the tip (F_N) are balanced by repulsive forces, which is the reciprocal load force of the sample (F_L). Inset of the AFM diagram shows a two spring model, where one spring is derived from the spring constant of the tip (k_{cb}), causing the tip to bend; the other is from the elastic properties of the sample (k_i). Inset of the COIFM diagram shows a single spring model, where the spring is due to the elastic properties of the sample (k_i) because there is minimal cantilever compliance as a result of the COIFM's feedback.

2. DESIGN CONCEPT AND SET-UP

The conventional atomic force microscopy (AFM) has used a flexible cantilever to have higher sensitivity and to make the probe less invasive to soft sample surfaces. However, this approach has a drawback in high-speed imaging on these surfaces: Assuming that the biological sample can be considered as a soft medium with viscoelastic properties, a typical

transient response of the cantilever with time (t) for a disturbance force during the force-feedback can be described by a simple exponential decay function or $1 - \exp(-\omega_0 t / Q)$, where ω_0 is an angular frequency at resonance and Q is quality factor [28, 29]. Since the imaging speed is determined by the decay constant $\tau = Q / \omega_0$, the lower resonance angular frequency of the soft cantilever causes the slow imaging speed. To improve the imaging speed, either the resonance frequency or the spring constant should be large. However, by using a smaller-sized cantilever to increase the spring constant, force-sensitivity is degraded and issues arise with fabrication and signal detection with a smaller laser spot size. Because the COIFM has zero compliance or Δz equals zero, the spring constant defined as $k = \Delta F / \Delta z$ according to Hooke's law (i.e., $F = k \cdot z$) becomes infinite. While the decay constant becomes infinity, thus the decay time becomes zero. Therefore, the COIFM is an ideal example of how to make the spring constant larger, because the spring constant can be considered infinite due to the counter force. This means that the cantilever is able to respond quickly by employing a feedback scheme to induce a counter force. Also, the HSAFM can retain a normal size and therefore, consequently avoid the force sensitivity, fabrication, and signal detection issues that are related to smaller cantilever sizes. This concept leads to our novel force-feedback HSAFM system for fast biological imaging.

The COIFM was originally developed to overcome the limited ability of AFM techniques to detect the static force at a few nanometers above the attractive surface due to mechanical instabilities of the tip-sensor assembly called the "snap-to-contact" phenomenon [18-21]. This phenomenon corresponds to the sudden transition from the noncontact to contact states in contact mode AFM [21]. The transition is caused by the uncontrolled movement of the probe to the surface when the intermolecular force gradient ($\partial F / \partial z$) exceeds the spring constant of the force probe (k). The contact mode AFM is unable to image topographic structures of the surface in the noncontact regime due to this mechanical instability.

To avoid the snap-to-contact phenomenon, traditionally amplitude modulation (AM) AFM has been employed to image soft samples or to visualize electric or magnetic structures, which generate long-ranged electric or magnetic forces. Kühle et al. found that several points of instability in the parameter space caused by attractive forces combined with repulsive elastic-type forces resulted in disturbances during image acquisition on hard elastic surfaces [30]. The amplitude modulation (AM)-AFM images generated some protruded artifacts when the probe encountered the high hillock structures. These features were interpreted as nonlinear stochastic phenomena in the tip-sample interactions [31]. The abrupt changes in the height of topographic features were associated with the continual switching of the oscillating tip between the two stable states while the tip scanned the surface in the AM-AFM [31-33]. Similarly, the topographic features in the magnetic image are attributed to the switching between the bistable states in magnetic force microscopy (MFM) [34]. This concept has been applied to separate the topographic structure from magnetic images using electrostatic modulation. In principle, both effects of the AM-AFM and MFM result from the intrinsic nonlinear mechanical bistability of the sensor-sample assembly. In the COIFM system, the snap-to-contact issue associated with contact mode AFM due to the bistability was removed using voltage-activated force feedback [15, 35].

We utilized our existing COIFM system capability (originally designed for interfacial force measurements) as a base to develop our force-feedback system [22]. The force-feedback

HSAFM requires 1) fast response of the force-feedback loop; and 2) capability of tracking large topographic features with heights greater than 200 nm on biological surfaces. This fast response was realized due to the high-resonance frequency of the cantilever with a built-in actuator (a bimorph stack). Tracking larger topographic variations was accomplished by employing a conventional piezo tube.

Figure 2 shows the conceptual design of the force-feedback HSAFM and how it operates during the imaging process step-by-step. When the tip encounters a larger topographic feature of a biological sample during scanning (see step 1), the force exerted upon the tip causes it to bend upwards (see step 2). An error signal (V_{Error}) generated by the bending motion of the cantilever is removed by a counter force applied to the self-actuating cantilever through force-feedback (as shown in step 3). Additionally, the signal is sent to the piezo tube through another feedback loop. It is important to note that both the actuations of the cantilever and the piezo tube can occur simultaneously and cooperatively. However, the response time of the piezo tube is roughly ten times slower than the cantilever and therefore the high speed imaging rate is mainly limited by the response time of the feedback loop that involves the piezo tube. The response time corresponds to the transition time from step 3 to step 4, where the piezo tube has moved down to release compression and deformation of soft biological samples.

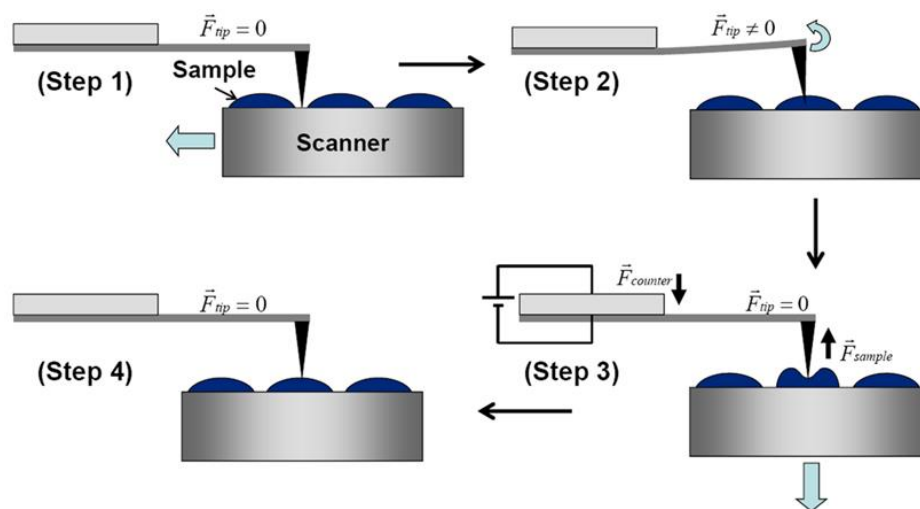


Figure 2. Conceptual diagrams for the principle behind the force-feedback HSAFM. The tip is in contact with the sample surface without bending of the cantilever (Step 1). The tip encounters the biological structure when the sample moves laterally, causing the tip to bend (Step 2). When a voltage is applied to the ZnO stack due to the force feedback, the counter force compresses and deforms the biological structure (Step 3). The biological structure is released from compression and deformation, as the sample moves down vertically due to the activation of feedback loop involving the piezo tube (Step 4).

We developed the force-feedback HSAFM using a commercially available cantilever called a “dimensional micro-actuated silicon probe” (DMASP) for both force-sensing and actuation for the force-feedback [22]. The DMASP cantilever has nominal dimensions of 55 μm width and 125 μm length [37]. These dimensions are larger by a factor of 5 than the

small-sized cantilever dimensions described in the introduction. By using this larger dimensional cantilever we can use ordinary AFM cantilever holder and laser beams for development with a conventional AFM system. This compatibility with the ordinary AFM will make the force-feedback HSAFM easy to adapt, avoiding the fabrication and signal detection issues associated with the use of small cantilevers. The DMASP probe contains a ZnO stack with a thickness of $3.5\ \mu\text{m}$ ZnO sandwiched between two $0.25\ \mu\text{m}$ Ti/Au layers, providing its nominal force constant of $\sim 3\ \text{N/m}$ [37]. This stack with the silicon cantilever has been used for fast imaging due to its higher-resonant frequency (nominally around $50\ \text{kHz}$ [37]) over the piezo tube actuator ($\sim 10\ \text{kHz}$) in ordinary AFMs [38-43]. The force-feedback loop consists of the DMASP, a feedback controller, and an AutoProbe LS head (Park Scientific Instruments) as shown in Figure 3. The DMASP sensor is wire-bonded to its built-in holder as received and is placed in the AFM cartridge for the laser beam alignment.

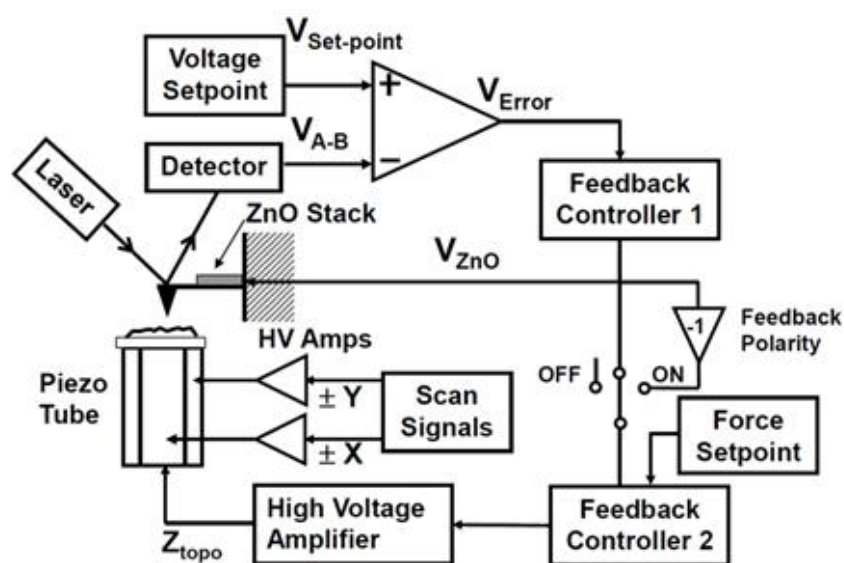


Figure 3. A schematic diagram of the force-feedback HSAFM system. The system employs an optical beam deflection-detection scheme, force-feedback loop, topographic feedback loop, and a piezo tube for X-Y-Z scanning and Z-feedback. The force-feedback HSAFM generates three different images: a deflection image (V_{A-B}), a topographic image (Z_{Topo}), and a force image (V_{ZnO}). Feedback controller 1 is for the force-feedback loop for force images, whereas feedback controller 2 is for the topographic feedback loop involving the piezo tube. The feedback ON/OFF and z-polarity switches are for enabling and disabling of the z-feedback loop and its polarity change, respectively.

A modified Burleigh STM controller (Burleigh Instruments Inc., Fishers, NY) was used as the force-feedback controller. The built-in optical beam deflection detection scheme was used to transmit the interaction force between the tip and the surface into the electrical signal [21]. In the laser beam deflection detection system, a position-sensitive photo-detector (PSPD) was adjusted to align the laser beam (deflected from the cantilever) to be positioned at its center. The PSPD output (V_{A-B} signal), was connected to the feedback input of the controller. The feedback control parameters, such as time constant and gain, were manually adjusted for the optimal feedback condition. The output of the feedback controller was sent directly to the ZnO stack of the DMASP to apply a counter force to the cantilever. The

actuation function of the DMAPS was used to control the force applied to the cantilever to maintain the constant deflection of the cantilever at a set-point value during the data acquisition.

An additional feedback loop involving the piezo tube was developed for large-scale topographic imaging capabilities [22]. In the feedback loop, the output of the force-feedback controller was fed through an RHK SPM 100 controller (RHK Technology Inc. Troy, MI) via an ON/OFF switch (see Figure 3). The output of the RHK controller was sent to the z-electrode of the piezo tube via high voltage amplifier ($\times 22.5$). The feedback loop maintains the force signal constant by changing the tip-sample spacing up to $\sim 2.5 \mu\text{m}$ or minimally $\sim 1 \text{ pm}$ in the z direction depending on the actuation range of the piezo tube and the voltage range and precision of the RHK controller, respectively. This allows the piezo tube to sufficiently follow typical biological cells. The voltage applied to the piezo tube was recorded as a topographic signal for each AFM image displayed. Due to the involvement of the feedback loops these images can also be inferred as representing a constant-force image [24]. These set-force dependent constant force images were obtained by changing set-force in Figure 3. The system is capable of interpreting the observed constant-force images, by capturing two additional images: force and deflection images.

All data was recorded through analog-to-digital converter (ADC) inputs of the RHK 100 and XPM PRO software [22, 24, 27]. The X and Y scanners of the piezo tube were used for the sample movement, which were controlled by digital-to-analog converter outputs, the inputs of a high-voltage amplifier. The maximum scanning area of the system is $100 \mu\text{m} \times 100 \mu\text{m}$. For the collection of force-distance measurements, the force-feedback voltage (V_{ZnO}) was recorded as a function of distance between the probe and the sample surface during both approach and retraction of the piezo tube [15, 17]. Force-distance curves are obtained under the off-feedback condition by sweeping the computer-controlled input of a z high-voltage amplifier. For force-distance measurements, an appropriate position of the z-feedback polarity switch of the RHK controller is selected, depending on the sign of the slope desired at a chosen set force in the force-distance curve; however, during AFM imaging the z-feedback polarity switch remains in the off position. For the collection of force-distance and deflection-distance curves, the force-feedback voltage (V_{ZnO}) and the deflection voltages ($V_{\text{A-B}}$) are recorded, respectively, as a function of distance between the probe and the sample surface during both approach and retraction of the sample [15-17]. The conversion factors of 5 nN/V and 49 nm/V are used to convert voltages of V_{ZnO} and $V_{\text{A-B}}$ into normal-force scale and deflection-length scale, respectively [16]. Because the breakdown voltage of the ZnO actuator DMAPS is nominally $\pm 10 \text{ V}$ [37], the controller output was designed to be saturated for the force variations larger than 50 nN during the data acquisition.

3. EXPERIMENTAL

In substantiating the proof of concept [22], verifying the ability to measure mechanical properties [24], and to study the stability [27] of the force-feedback HSAFM, all data was collected on an oxidized silicon two-dimensional grating sample with $10 \mu\text{m}$ periodicity (laterally) and 180 nm step height acquired from Veeco, Inc. [44]. The $10 \mu\text{m}$ periodicity and

180 nm step height of the grating sample were used for an additional dimensional scale for each collected image.

To demonstrate the system's applicability to biological samples in the proof of concept and stability study, an *Escherichia coli* (*E. coli*) culture and biofilm sample were taken from a PBS solution and deposited onto the clean grating structure [22, 27]. The culture of a non-pathogenic strand of *E. coli* (RK4353) was grown overnight with shaking (225 rpm) at 37°C in 5 mL of Luria Bertani broth. The culture was pelleted at 6000xg/10min, and resuspended in sterile PBS. 1 mL of the mixture was then dispensed into 99 mL of fresh PBS solution, causing a 1:100 part dilution. During high-speed AFM imaging, the set force of ~0 nN was utilized with the activation of the feedback loop.

The sample was surveyed using the optical imaging of a vertically placed, charge-coupled device (CCD) camera with two different objective magnifications (20× and 80×), before and after dropping 1 mL of the diluted *E. coli* and related biofilm solution on the grating sample. The lower magnification provides a large overview of the dispensed material, whereas the higher magnification provides a detailed view within the dispensed material. Deflection, force, and topographic images were taken at 0 nN set-force for various scan speeds and scan sizes on biofilm and *E. coli* samples.

In the verification of the ability to measure mechanical properties, a soft film was grown on the grating sample by exposing it to the ambient environment for 60 days at a relative humidity of approximately 10-20% and a room temperature of 22°C [24]. Most studies of micromachines exposed to prolonged periods in the ambient environment are concerned with the effects of water more so than the effects of ambient formed hydrocarbon thin-films [45-52]. AFM images, taken with an AutoProbe LS AFM system (formerly Park Scientific Instruments) using a Veeco NP-20 probe [37], were used to study the structure of the layer. Another soft hydrocarbon film was later grown on the grating sample at a relative humidity of 30% and a room temperature of 22°C, by again exposing the grating sample to the ambient environment for 60 days to study into the ability of the force-feedback HSAFM [27]. The ambient material allows for the covering of the hydrophilic grating sample with a layer consisting of hydrophobic properties [37]. Topographic and force images were taken with alternating positive and negative applied-forces. Before deposition of ambient films or biological samples and after data acquisition, the grating sample underwent a cleaning procedure consisting of submersion into a piranha solution made from a 3:1 concentrated H₂SO₄/30% H₂O₂ (Pharmco and Fischer Scientific, respectively); then sonicated in acetone, ethanol, and distilled water for 5 minutes in each; and ultimately dried with an N₂ flow. This allowed for comparison and correlation of the effects of hydrophilicity.

4. HIGH-SPEED IMAGING

The main aspiration of the design and development of the force-feedback HSAFM stemmed from the need for a tool capable of large-scale high-speed topographic imaging of delicate material, such as biological samples; thus, to prove the concept of the system, high-speed imaging was taken on *E. coli* biofilms [22].

Figures 4(a) and 4(b) show lower and higher magnification optical images, respectively, before applying the *E. coli* biofilms on the clean grating sample surface. The square-like

periodic patterns are clearly visible. These patterns provide not only the reference to determine if the *E. coli* film is deposited, but also give a scale for the images of interest. Figure 4(c) shows a low-magnified optical image of the *E. coli* biofilms on the sample surface. Large pyramidal-shape structures were observed in the optical image, which are most likely artifacts due to the crystallization of ions in the PBS solution as the solution dried. Figure 4(d) shows a higher magnified optical image of the *E. coli* biofilms on the sample surface. By comparing the before and after images, it was evident that material had been trapped in the grating indents. Therefore, the optical images allow for the tip to be moved to a desirable location to be compared with the high-speed images to understand the general distribution of the films.

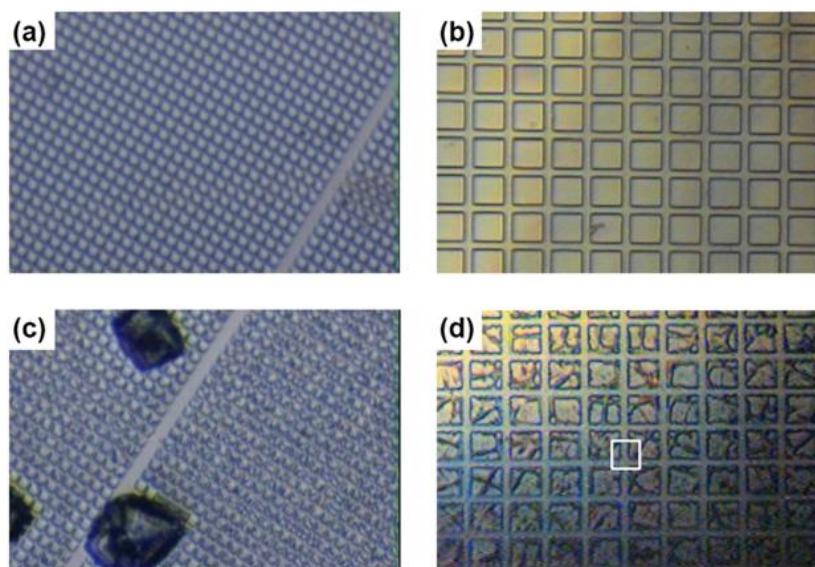


Figure 4. Magnified optical images of a clean two-dimensional grating with 10 μm periodicity using a 20x objective lens (a) and an 80x objective lens (b). Magnified optical images of *E. coli* bacteria and their biofilms deposited on the grating using a 20x objective lens (c) and an 80x objective lens (d). *E. coli* biofilms in the PBS solution were collected, deposited, and dried on the grating surface. A square outlined with white lines is the area where the images were taken subsequently by the force-feedback HSAFM.

The principle of force-feedback HSAFM was tested by imaging biological samples with large height variations on a two-dimensional grating with 10 μm periodicity [22]. The tip was scanned in a square outlined with white lines, as seen in Figure 4(d). Minimal signal changes of less than 1 nm were exhibited in V_{A-B} , as shown in Figure 5(a). This is due to the actuation voltages being applied to the piezo tube and the ZnO stack, as displayed in Figure 5(b) and Figure 5(c), respectively. This result suggested that both force-feedback and the piezo tube work together to make V_{A-B} approximately zero. The minimal signal change in the “deflection image” from V_{A-B} of Figure 5(a) and its underlying sectional profile (taken at the dashed line) suggested the feedback loop is efficiently working to compensate for the error and that the system is following the sample topographic variations accurately. Since the feedback voltage applied to the piezo tube is related to the topographic height at a specific point on the surface, Figure 5(b) represents a “topographic image.” The image was taken on the biological surface

with a scan area of $8\ \mu\text{m} \times 8\ \mu\text{m}$ at a scan speed of 0.4 frames per second and a V_{A-B} signal condition of zero. Part of the periodic grating structure (see in Figure 4) can be observed on the topographic image. The sectional profile in Figure 5(b) shows that the topographic height variations ranged 300-400 nm during high-speed imaging. It appeared that the biofilm and its corresponding extracellular polymeric substance have been trapped in the lower part of the grating sample, as seen by the large feature with a sudden increase of topographic height. Fine structure roughness was evident on the surface of the biofilm as seen by the elevated texturing of stripe-like features along the diagonal direction of the surface with a periodicity around $\sim 500\text{-}800\ \text{nm}$ with a height of $\sim 50\ \text{nm}$. The biofilms appeared to be buckled due to the grating structure and in an “L”-shape. The flat area was the upper terrace of the grating sample, where the diameter of some small structures (most likely debris from the biofilm from transplantation process) ranged between 10 nm and 30 nm. The biofilm appeared to be unevenly spread out, which is confirmed by the underlying sectional profile of biofilm (with a topographic height of $\sim 180\ \text{nm}$) and grating sample at the dashed line. This showed that the force-feedback HSAFM follows subtle structural variations accurately.

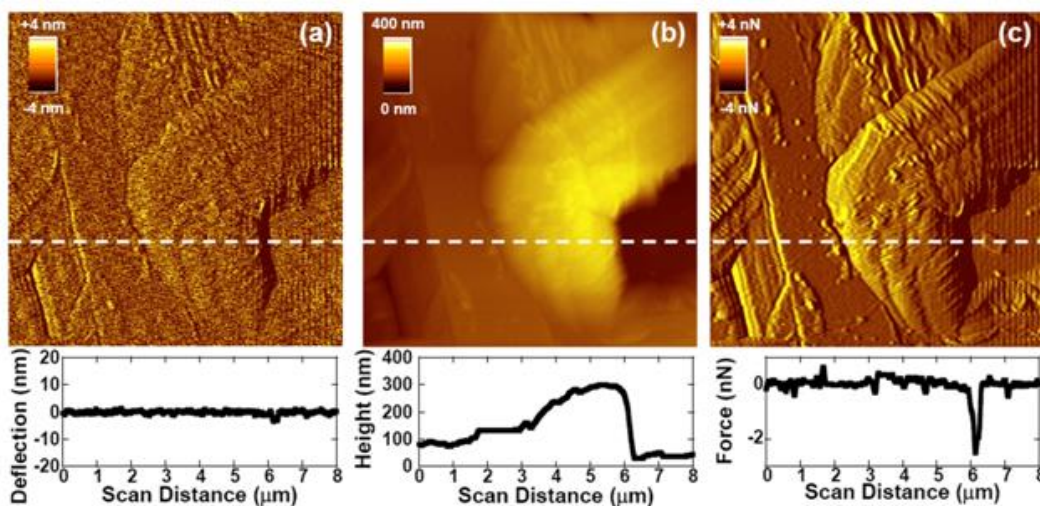


Figure 5. Three images taken by the force-feedback HSAFM on the *E. coli* biofilms on the grating. (a) Deflection image (V_{A-B}). (b) Topographic image (Z_{Topo}). (c) Force image (V_{ZnO}). Images were collected at 0 nN set-force on the grating structure at a scan rate of 0.4 frames per second. The scan area is $8\ \mu\text{m} \times 8\ \mu\text{m}$ with 128×128 data points. The lower panels represent sectional profiles taken along the dashed lines.

Figure 5(c) represents a “force image” from the V_{ZnO} , a force-feedback signal in conjunction with topographic feedback to compensate for the V_{A-B} signal shown in the deflection image, Figure 5(a). Interestingly, the image showed an enhanced contrast over the topographic images, especially near a boundary where the two different structures meet, allowing for clearer visualization of the small features just described in relation to Figure 5(b). This idea was supported by the fact that the underlying sectional profile of Figure 5(c) showed one large valley indicating a large topographic change. When the force sectional profile was related to the topographic sectional profile, the large valley in the force signal was suggested to be due to the large topographic height of the biofilm decreasing abruptly to that

of the lower terrace of the grating sample. The result suggested that the sudden signal changes near such abrupt structures are too fast for the topographic feedback involving the piezo tube to attain the set-force through the removal of the feedback error. The minimally observed change in the deflection image indicates that these uncompensated signals are delivered and compensated by the force-feedback involving the fast cantilever to make the deflection signal stay constant. Therefore, both feedbacks worked cooperatively in cancelling the deflection signal in response to the surface variations, as discussed in diagrams of Figure 2. The force-feedback loop allowed the self-actuated cantilever to respond rapidly, while the topographic-feedback loop permitted the piezo tube to relieve the compression and deformation created by the cantilever to attain a constant force on the cantilever through another feedback (see steps 3 and 4 in Figure 2). It seemed that this cooperative feedback compensation enabled the cantilever to follow the topographic features of biological samples with negligible bending.

The capability of the force-feedback HSAFM was determined by observing how different imaging rates influence the imaging of the biological sample [22]. Topographic images and their simultaneous force images taken under different imaging rates are displayed. Figures 6(a) and 6(b) show the images taken at 0.04 frames per second. The images were taken over a segment between two of the periodic indentations, which appeared to be covered by a layer of biofilm. Denser individual clusters within the biofilm were evident by pockets of higher topographic elevation; however the biofilm was less compact than in Figure 5. The dense clusters in the thin film had a height of ~ 100 nm and a diameter ranging from ~ 20 – 40 nm (as seen in the underlying sectional profiles in Figure 6). It is interesting to note that the denser portion of the film that is trapped in the lower left grating indentation with the oscillating-wave-like texture had a height of ~ 200 nm. This indicated that the denser the biofilm, the more the internal cells aggregate and the higher the achieved topographic height. The lower right indentation was also covered by a thin film (~ 40 nm height), so thinly layered that there were pockets where the height was merely ~ 10 nm (in the dark strip with diameter of ~ 800 nm), although the film got progressively larger near the upper terrace (~ 200 nm height from the ~ 40 nm). In the top section of the upper terrace, small structures could be seen with heights of ~ 20 nm and diameters of ~ 10 – 50 nm (as seen previously in Figure 5, these small features were presumably parts derived from the biofilm during transplantation).

The high-resolution topographic imaging was not degraded at all as the scan rate was increased from 0.04 frames per second to 0.1 frames per second. Most of the force images showed that the force was constant on the upper terrace on the grating except when abrupt signal changes occurred due to small features. However, when imaging rate was accelerated, force image became rougher due to the limiting capability of the piezo tube's response to the rapid signal change. In contrast to the topographic image, the force image (Figure 6(b)) again showed better contrast, which can be used as complementary information in understanding the delicate structural change on the biological surfaces. This was again due to the residual force signals that were not compensated by the topographic feedback loop due to the abrupt change in the sample's mechanical property or rapid topographic changes. This type of image is analogous to the frictional force image and in contrast to the topographic image where the sample's boundaries were always emphasized [53, 54]. For example, those delicate features in the force image cannot be easily identified with topographic images only. Figures 6(c) and 6(d) show the topographic and force images, respectively, taken at the same location with a different scan rate of 0.1 frames per second. No notable changes were discernible, except the appearance of a small y-axis striation pattern on the right side in the force image in Figure

6(d). The striation pattern has been observed previously and has been found to be the result of the piezo tube approaching resonant vibration frequency (e.g., [1, 4, 55-57]). The pattern became more dominant as the scan rate increased. Figure 6(e) and Figure 6(f) are the topographic and force images, respectively, taken with the scan rate of 0.2 frames per second. Both images show a larger striation pattern parallel to the y-axis. The images taken at the scan rate of 0.4 frames per second, (Figure 6(g) and Figure 6(h)) exhibit a greater increase in the striation pattern, particularly more prominent in the force image. Additionally, the underlying inset of Figure 6(g) shows decreased sensitivity to minute topographic variations. At 2 frames per second (image not shown), features became too distorted to be accurately distinguishable due to the interference of the pattern in resolving the features on the images. The result suggests that the scanner resonance frequency is an important limiting factor in dictating the speed limitations of the force-feedback HSAFM.

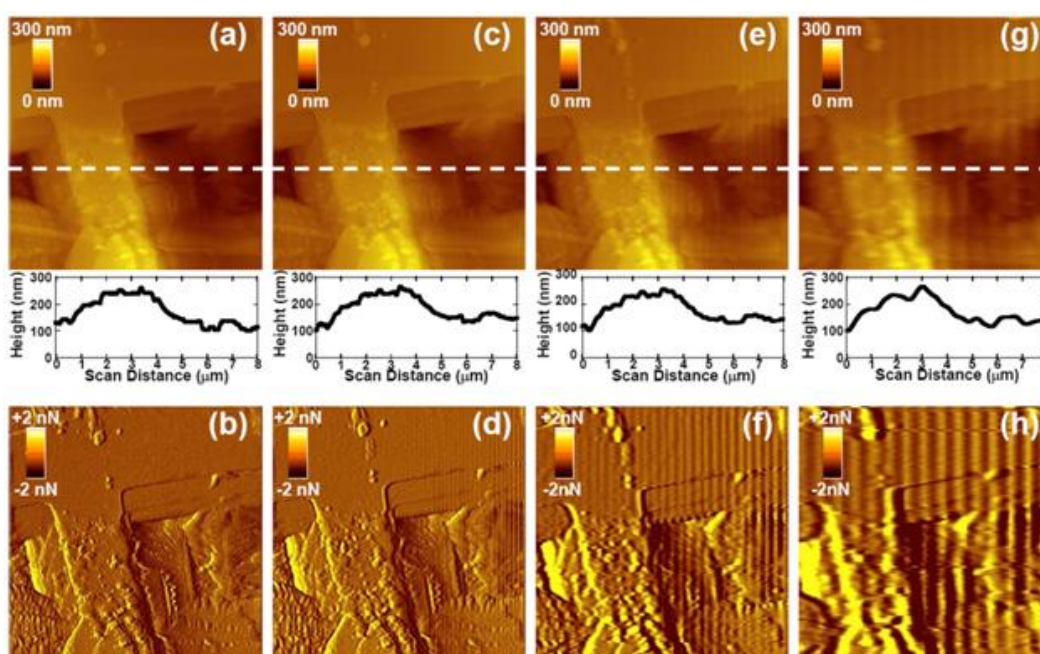


Figure 6. Topographical and force images collected simultaneously at 0 nN set-force on the *E. coli* biofilms at four different scan rates: 0.04 frames per second (a, b), 0.1 frames per second (c, d), 0.2 frames per second (e, f), and 0.4 frames per second (g, h). The scan area is $8 \mu\text{m} \times 8 \mu\text{m}$ with 512×512 data points. Underlying sectional profiles of the topographic images are taken at the dashed white line.

The invasiveness of the system during high-speed scanning was then tested on biological samples by imaging what appeared to be a single cell of *E. coli* on the grating sample (highlighted by the squared section) at different imaging rates [22]. Figure 7(a) shows an $8 \mu\text{m} \times 8 \mu\text{m}$ high resolution topographic image and Figure 7(b) shows the corresponding force image, taken at 0.8 frames per second, of what appears to be a sequence of step-like biofilm structures (with each step height of $\sim 200 \text{ nm}$) developed during the sample preparation. The image contains a small rod-shape about $2\text{-}3 \mu\text{m}$ long and about $0.5 \mu\text{m}$ in diameter in the lower right corner. We considered the structure as a lone *E. coli* cell because the dimension and morphology is consistent with the literature values of *E. coli* [28]. We zoomed in on a

squared area ($2.5 \mu\text{m} \times 2.5 \mu\text{m}$) outlined by white lines. Figures 7(c) and 7(d) shows topographic and force images collected simultaneously on the bacterium at an imaging rate of 0.08 frames per second. As expected with this scan rate, the images did not show any visible striation pattern.

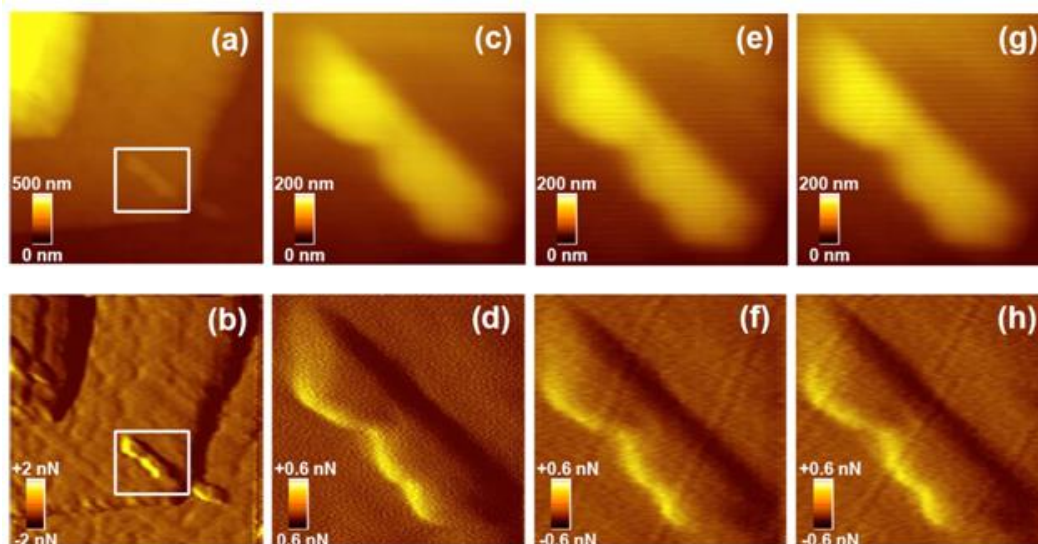


Figure 7. Topographical image (a) and force image (b) collected simultaneously at 0 nN set-force on the *E. coli* biofilms collected in the scan area of $8 \mu\text{m} \times 8 \mu\text{m}$ with 128×128 data points. The scanning rate was selected to be 0.8 frames per second. Topographical and force images collected simultaneously at 0 nN setforce in a reduced scan area of $2.5 \mu\text{m} \times 2.5 \mu\text{m}$ to have a magnified image of an *E. coli* bacterium. Topographic and force images taken at 512×512 data points at a scan rate of 0.08 frames per second (c, d), at 128×128 data points at a scanning rate of 0.8 frames per second (e, f), and at 128×128 data points at a scanning rate of 1.6 frames per second (g, h).

The *E. coli* was shown to have the characteristic smooth texture for the cell surface with a small indentation in the center of the cell. This difference in smoothness from those seen in the images of biofilm appeared to be due to cell morphology being physiologically different when a cell is grown in a biofilm compared to a planktonic cell (freely floating cell) of the same organism [28, 29]. When we increased the speeds to 0.8 frames per second (see Figures 7(e) and 7(f)), force images did not show the striation pattern along the vertical y-direction. Interestingly, the striation pattern was again not visible when we increased the scan rate to 1.6 frames per second (see Figures 7(g) and 7(h)). It appeared that the striation pattern was also dependent on the scan size as well as the scan rate, which is most likely due to the redirection of higher momentum when imaging a larger scan size at the same imaging rate (1 frame per second). Since with larger scan sizes more distance must be covered in the same amount of time, the velocity while scanning must be greater. Therefore, the impulse or momentum change is greater when imaging at larger scanning sizes. The images of the *E. coli* were reproducible without showing any observable change of the *E. coli* structure even with the scan rate changes by a factor of five. This reproducibility indicated the absence of major deformation of the sample during the successive scans. This may be related to the fast response of force feedback between steps 3 and 4 in Figure 2. Additionally, if the set-force

applied to the cantilever during (step 3) is set very large then the sample, if soft, could be damaged; however, under normal set-force values the force-feedback is so rapid that it can effectively control the spring constant of the cantilever to allow it to become very compliant. Because of this mechanism, this system is far superior in regards to not damaging sample surfaces in comparison to using a small stiff cantilever to reach high speeds. The interaction between a probing tip and a delicate surface (e.g., between a tip and gram-negative bacteria, which have a thin peptidoglycan layer compared to that of gram-positive bacteria) is known to even sometimes be irreproducible with conventional AFM imaging [60].

The cantilever resonance frequency was concluded to be the determining factor for the time scale of the DMASP cantilever in comparison with that of the piezo tube [22]. Figure 8 shows a plot of the amplitude of the response signal as a function of the frequency measured with a lock-in amplifier. A driving signal with an 50 mV amplitude was applied to the set-point input ($V_{\text{Set-point}}$ in Figure 3) for its frequency range between 1 Hz to 50 kHz (TEMA: 2 MHz function generator). One of the ADC inputs of the RHK 100 controller was used to record the measured amplitudes [34]. The measured mechanical response data was fitted with

a classic second-order mechanical response, $\frac{(G_{\text{ZnO}} \cdot \omega_0^2)}{\sqrt{(\omega^2 - \omega_0^2)^2 + 4(\zeta\omega_0\omega)^2}}$; where

G_{ZnO} is dc gain constant, ζ is the damping ratio and ω_0 is the natural resonance frequency. The solid line in Figure 8 is the curve fitted with the parameters with ζ of 3.5×10^{-3} and ω_0 of $2\pi \times 42.6$ kHz. The G_{ZnO} was found to be 34.07 mV/V from the slope between the deflection signal ($V_{\text{A-B}}$) and the ZnO voltage signal (V_{ZnO}), which was measured in advance (solid line in inset of Figure 8).

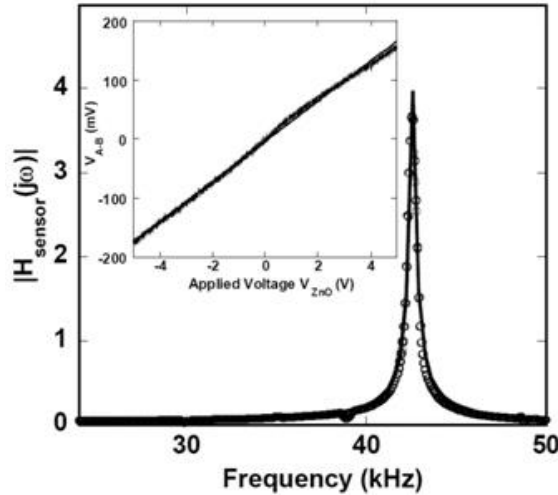


Figure 8. A plot of the amplitude of the output voltage ($V_{\text{A-B}}$) as a function of frequency (f) of the sinusoidal driving voltage applied to the ZnO stack (solid line). The data was fitted with a classic second-order mechanical response to find the resonance frequency and damping constant. (inset) The deflection signal $V_{\text{A-B}}$ as a function of the applied ZnO voltage signal (V_{ZnO}) for the range between -5 V and +5 V under the inactivation of force-feedback loop. The curve provides the dc gain constant G_{ZnO} .

The cantilever resonance frequency of 42.6 kHz mainly determined the bandwidth, as the bandwidth of the force-feedback controller is higher than 200 kHz [22]. The shortest response time of the force-feedback is the inverse of the resonance frequency or $1/f_0 = 23.4 \mu\text{s}$. For the piezo tube, the resonance frequency was calculated from the observed striation pattern in Figure 6(d). Because the number of patterns is ~ 15 and the tip speed 1.6 frames per second, the periodicity was determined to be 0.33 ms. This result corresponded to a 3 kHz resonance frequency in the x-y direction for this scanner. According to Zareian Jahromi et al., the axial resonant frequency tends to be approximately 3 to 3.5 times that of the bending resonant frequency [61]. The axial resonance frequency is determined by ~ 10 kHz for this scanner. The shortest response time of the piezo tube is $\sim 1/f_0 = 100 \mu\text{s}$. So for example, Figure 7(a) has 128 data points per each line; the shortest time to complete a line scan is 12,800 μs . The fastest scan rate possible is 0.6 frames per second, which is roughly consistent with our observed scan rate of 10 ms per line. This consistency confirms that the low-resonance frequency of the piezo tube is the limiting factor that determines the bandwidth of the current force-feedback HSAFM. The imaging speed of the force-feedback HSAFM would be improved by using the piezo scanner with high-resonance frequencies such as conical piezo tubes [62].

Even with the use of a larger cantilever over the smaller-scale cantilever, the force-feedback HSAFM achieved high-speed imaging through the fast force-feedback mechanism [22]. The spring constant is considered relatively infinite when combined with the force-feedback scheme. The force-feedback, to maintain the cantilever deflection constant, allows for faster response to topographic variations. Due to the cooperativeness between the force-feedback loop and the piezo tube feedback loop, the system is able to capture distinguishable biological features at high-speeds inaccessible prior.

5. MECHANICAL PROPERTY IMAGING

AFM has been widely used in mapping topographic structures and mechanical properties, such as viscoelastic and adhesional properties [25, 44, 53, 54, 63-76]. Force-modulation AFM techniques were introduced two decades ago to image topographic, elastic, and viscous images at the same time [25, 53, 53, 70-72, 74, 76]. This simultaneous imaging was realized by separating the signals in the frequency domains. This method has been applied to various materials including a living cell (live platelet) [25], carbon fiber and epoxy composite [72], self-assembling monolayers (SAMs) of organic thiols (terminated polystyrene) on gold [63], nickel-based superalloy (MC2) [71], and cold plastic [70]. Such modulation techniques have been extended to acquire electric properties of materials, such as ferroelectric domains [77-80]. However, the topographic image and its complementary images acquired through the modulation technique are difficult to interpret because of the complex dependence of those images on the amplitude and phase of driving signals due to the nonlinear nature of tip-sample interaction in the contact regime.

In comparison to the previously mentioned modulation methods, topographic and mechanical images based on dc-measurement techniques have been interpreted in a more straightforward way [68, 69, 73, 75]. Tip force was measured as a function of distance for each tip position for mapping of adhesional profiles on the sample surface. For the adhesional

mapping, pull-off forces were extracted from force-distance curves measured for all data points over the scan area, and were displayed as a single image along with the topographic image to find their correlation. For elastic modulus images [69], the indentation portion of the force-distance curve was analyzed with classical contact mechanical models such as the Hertzian model to find the elastic modulus value for each tip location.

The newly developed force-feedback HSAFM was then applied to the double spring phenomena as a resultant of the tip stability issue that has plagued conventional AFMs when measuring mechanical properties of soft samples [24]. With the system's force-feedback scheme, it was hypothesized that any spring effect derived from the cantilever could be negated and the spring constant of the surface would be able to be isolated. As soft surfaces create their own forces due to their spring-like behavior, the study becomes complicated because of the double-spring effect where the cantilever acts as one spring and the adsorbed surface structure acts as another (see Figure 1(a)). The stiffness of sample (k_i) is related to the measured slope (k_m) by the following relationship [67, 81]:

$$k_i = k_m / [1 - (k_m / k_{cb})] \quad (1)$$

where k_{cb} is the cantilever spring constant. For quantitative measurement of the constant k_i , the cantilever spring constant must be deconvoluted from the measured data. However, the accurate calibration and determination of the constant k_{cb} are not generally straightforward [82]. This equation suggests that, when k_{cb} is infinite, the measured slope equals the sample stiffness. Also, this dc-measurement approach requires extensive data acquisition time from ~30 minutes to several hours [53, 69, 73], which sometimes causes unwanted problems such as severe drift, in particular, for soft materials including biological samples [75].

In the verification of the ability to measure mechanical properties, a soft film was grown on the grating sample as described in the Experimental section. A three-dimensional topographic view of the adsorbed material layer (lighter shaded) formed on top of the grating step (darker shaded) is presented in Figure 9(a). Granular structures with diameters of 300-500 nm, which appeared to form from a mixture of atmospheric compounds, such as water and hydrocarbons, were observed. A hydrocarbon film would be predominately derived from atmospheric methane hydrocarbons composites and non-methane hydrocarbons, primarily the result of fossil fuel combustion, and collectively being composed of propene, ethene, propane, etc. [83, 84]. The average thickness of the film was estimated to be approximately 50 nm (as marked with the double-headed arrow in Figure 9(a)).

To study the adsorbed material layer, deflection-distance and force-distance curves were collected simultaneously [24]. The deflection signal (Figure 9(b)) remained constant during both approach and retraction, confirming that the tip had zero compliance or infinite spring constant. All measurements of force-distance curves were collected at a tip speed of ~40 nm/s. Even though the tip interaction with a soft film coating could be dependent on the tip approaching rate, this is beyond the scope of the study. The force-distance curve (as seen in Figure 9(c)) displayed minute attractive force, implying that the outer surface of the adsorbed material has hydrophobicity. Because the majority of air molecules are nonpolar, the nonpolar hydrophobic surface preferred to orient outward to be exposed to those ambient nonpolar molecules. If the sample's surface was hydrophilic, then thin water films that had formed on the surface would result in a slowly ramping attractive force before experiencing the sudden

large jump in attractive force in the force-distance curves [26]. However, if the tip was hydrophobic and approached a hydrophilic sample, then the force-distance curves would display a slowly increasing repulsive force before the tip comes into contact with the sample [85]. These characteristics were not observed in the force-distance data shown in Figure 9(c), thus confirming that the surface is hydrophobic in nature.

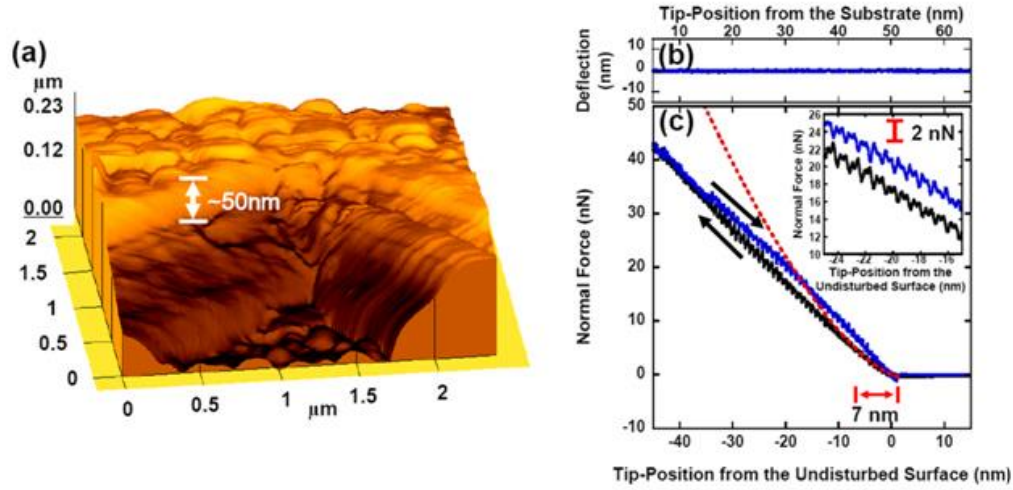


Figure 9. (a) A $2.3 \mu\text{m} \times 2.3 \mu\text{m}$ three-dimensional AFM image of the $10 \mu\text{m}$ periodicity grating structure after being exposed to the ambient environment for approximately 60 days, taken at an imaging rate of 0.004 frames per second. The average thickness of the adsorbed material layers is ~ 50 nm, demonstrated by the lighter layer above the dark section as indicated by the double headed arrow between two white lines indicating silicon surface height and adsorbed material height. (b) Graph of deflection signal (V_{A-B}) compared to the relative tip-position from the silicon substrate or tip-position from the top of the adsorbed material film. (c) Force-distance curves between the tip and the grating structure, with a force-activated-voltage-feedback system during approach and retraction measured at 11% relative humidity. The zero point position for the lower x-axis (used in the text) of both the force-distance and deflection graph was defined as where the probe came into contact with the adsorbed layer. The zero point position for the upper x-axis was defined to be at the surface of the silicon substrate, which the adsorbed material covers. The dashed fitted line represents a fitting of the approach curve with the Hertzian model for the range indicated by the double arrow between the two small vertical lines. The inset shows a zoomed-in sectioning of the force-distance curve.

The force-distance approach curve (Figure 9(c)) displayed a nonlinear behavior before the steep linear increase [24]. The nonlinear behavior was able to be explained with the Hertzian model, which describes the relationship between the applied load and the contact area between a spherical tip and an elastic sample surface when they are being pressed against each other. Fitting the non-linear section of the approach curve (from approximately 0.2 nm to -6.8 nm) with the Hertzian model equation [26, 86, 87]:

$$F = \frac{4}{3} E \sqrt{R} \delta^{3/2} \quad (2)$$

where the force (F) is related to the elastic modulus (E), the radius of contact (R) of 10 nm [37], and the indentation depth (δ), allowed for the determination an E value of 54 ± 2 MPa

with a correlation coefficient of 0.98073. When indentation depth was comparable to the tip radius, the force curve followed the Hertzian model; however, when the indentation depth was larger than the size of contact, the force increased linearly (as seen in Figure 9(c) after a 10 nm indentation depth). The force changed linearly with distance once the tip came into full contact with the surface. The sample compliance was found to be ~ 1 N/m. The sawtooth-like oscillation pattern in the linear section pointed to possible layered structures. Whenever the tip-repulsive force exceeded the covalent bond strength, the tip punctured each internal film layer [87]. The rupturing force of the layers (as seen by the inset in Figure 9(c)) was between approximately 1 nN to 2 nN, which was consistent with earlier observations of silicon-carbon covalent-bond-rupturing forces [88]. This oscillatory pattern indicated the existence of layered structures built during the process of film formation.

To investigate the mechanical properties of the internal material, the tip was used to agitate the adsorbed material [24]. The tip was forced to penetrate the adsorbed material by applying a set-force value of 2 nN, high enough to overcome the tensile strength of the adsorbed film. Then the tip was invasively scanned repetitively at the high speed of 2.5 $\mu\text{m/s}$ with the use of the feedback mechanism. Deflection and normal force signals were measured simultaneously during tip approach and retraction to understand the internal mechanical properties of the adsorbed layer.

The deflection–distance curve (Figure 10(a)) confirmed that the deflection remained constant due to the force-feedback for all distances, except for those distances where a small peak and a small valley appear, as marked with vertical arrows. The peak and valley at ~ 9 nm and ~ 27 nm during approach and retraction, respectively, were due to the limited response time of the current force-feedback system to the sudden force changes. The result suggested that the force-feedback HSAFM has exceptional ability in isolating the force generated by the mechanical properties of the adsorbed material from the mechanical response of cantilever spring associated with AFM measurements. The force-distance curve (Figure 10(b)) showed that initially the tip did not experience any force until the tip and adsorbed layer joined together as shown in Figure 10(c).

On approach, the tip experienced a sudden attractive force of -7 nN due to the tip contact with the material surface (seen to be approximately 9.5 nm from the force-distance curve). The tip force then increased linearly as the tip-substrate distance decreased, causing the tip to push against the adsorbed material. When the tip retracted, the linear force followed the original approaching curves, indicating that the observed force is similar to a reversible process [24]. However, below the tip distance of zero, the adhesive force linearly continued until it reached 27 nm, when the attractive force rapidly increased toward zero and then slowed down near zero. The relatively large pull-off force (21 nN), in comparison to the attractive force (7 nN) on approach in the force-distance curve, indicated the existence of adhesive bonding between the tip and the adsorbed material. This strong adhesion signified that the adhesive internal parts of the adsorbed film were exposed to the ambient environment during the invasive scanning process. After the breakage of the adhesive bonding, van der Waals and electrostatic interactions were the only contributions to the observed attraction at the distance larger than 27 nm, as the distance increased. Based on the observation, the force-distance curves were divided into four regions: repulsive-contact (below 0 nm); attractive-contact (between 0 nm and 27 nm); attractive-noncontact (above 27 nm); and zero-force (above 30 nm) regimes (see Figure 10(b)). The adsorbed material between the tip and sample was modeled to form a meniscus-like column (see Figure 10(c)).

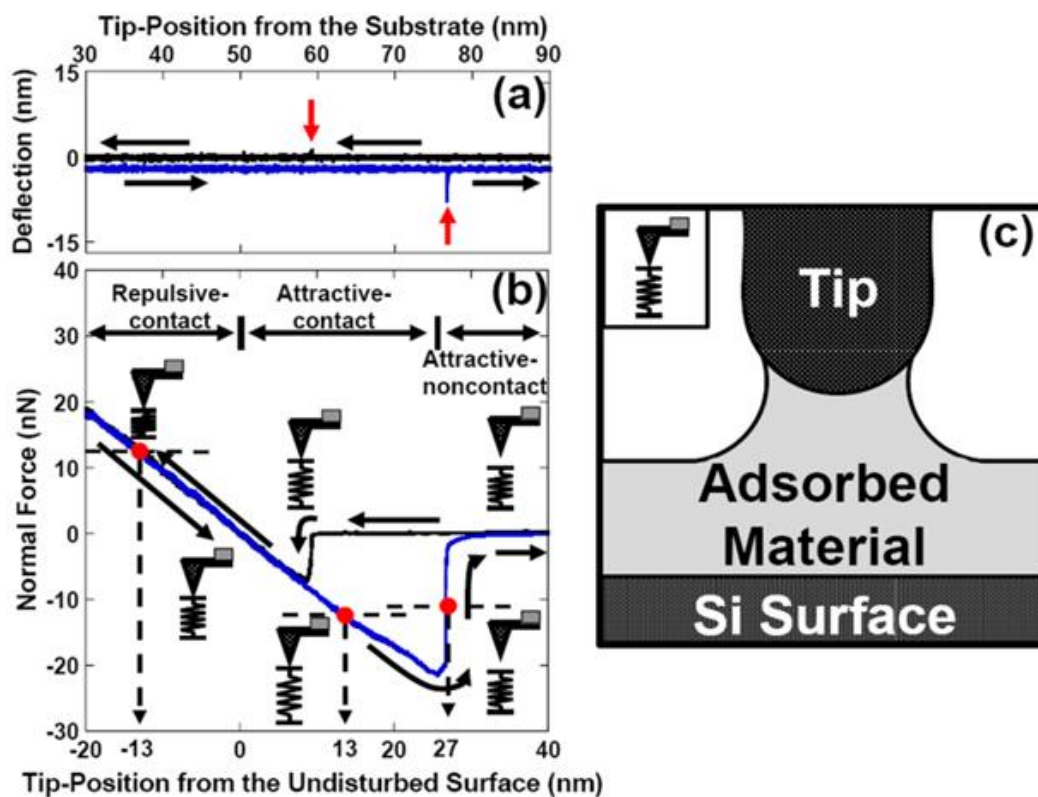


Figure 10. (a) Deflection and (b) force curves measured as a function of distance taken on the disturbed adsorbed material, during approach and retraction (each respectively marked) measured at 11% relative humidity. The zero position for the lower x-axis (used in the text) was described as where the probe came into contact with the top of the undisturbed adsorbed material. The other zero point for the upper x-axis is defined at the surface of the silicon substrate, in which the adsorbed material covers. The dashed lines are the set-point values of +1.25 nN (normal polarity), -1.25 nN (normal polarity), and -1.25 nN (reversed polarity). The solid circles on the force-distance curve intersect the dashed line in the attractive regime (negative force) and repulsive regime (positive force). The force-distance retraction curve is broken down into three separate regimes depending on force interactions: repulsive-contact, attractive-contact, and attractive-noncontact regimes. Spring models show tip and sample spring interaction at certain points in the force-distance curve. (c) Depiction of the meniscus-like column of the disturbed material between the tip and the surface. Inset shows that under this configuration the adsorbed material acts as an extended spring made of the column.

This force-distance curve suggested that the adsorbed material behaved like a linear spring that follows Hooke's law, as shown in the inset of Figure 10(c). The spring-constant (k_i) was measured to be 0.94 N/m from a linear curve fit on the portion from 10 nm to -50 nm. The stiffness of sample k_i was related to the elastic modulus E and the radius of contact R as follows:

$$k_i = fRE \quad (3)$$

where f was a geometric factor between 1.9 and 2.4 [89]. Using the k_t of 0.94 N/m, E was estimated to be between 40 MPa and 50 MPa, which was consistent with the value of 54 MPa, obtained with the Hertzian model above.

Spring models, in which the adsorbed materials on both the tip and sample surfaces were represented in each force regime, are displayed along the force-distance curve seen in Figure 10(b) [24]. On approach, once the tip came into close proximity of the adsorbed material layer, the attractive forces pulled the adsorbed material and the material coating the tip together to form a singular extended spring. When the tip reached the initial surface location of the undisturbed adsorbed material, the spring was in its relaxed state. As the distance continued to decrease between the tip and the substrate surface, the tip slowly compressed the material. As the tip retracted, it slowly decompressed the material until it passed the initial undisturbed starting position. The adhesive property of the material caused it to continue to cling to the tip as the tip continued to retract. Thus, the spring was stretched until the column was no longer able to maintain its adhesive bonding, separating and snapping back to its initial resting state.

Topographic images were obtained using the noncontact electrostatic interactions in the attractive-noncontact regime for constant-force imaging [24]. This topographic imaging method was effectively analogous to scanning polarization force microscopy [90]. By changing the z-feedback polarity at the set-force of -1.25 nN value, the tip was positioned around 27 nm above the surface of adsorbed material in the attractive-noncontact regime, as marked with the vertical dashed arrow in Figure 10(b). The resultant constant-force image (Figure 11(a)) exhibits a relatively smooth surface with the average roughness of only $\sim 5.6 \pm 0.9$ nm for the entire image (disregarding the step height of the grating sample). To determine average roughness, the root mean square (RMS) error was calculated for images using the image processing program, RHK XPMPro. Since the force did not remain constant in areas containing abruptly changing large structures (such as the grating steps), flat areas were only included for the calculations of the average roughness.

When the structure was imaged at the set-force of +1.25 nN in the repulsive-contact regime (Figure 11(b)), an average roughness was calculated to be $\sim 10.7 \pm 1.5$ nm, an increased value by a factor of 2. This roughness increase was also observed when imaging the same surface at the set-force of -1.25 nN in the attractive-contact regime (Figure 11(c)), with a resulting roughness of $\sim 10.6 \pm 2.2$ nm. This result indicates that the average roughness was dependent only on the existence of contact, not on the polarity of loading force. However, when three images were compared, some locations showed contrast variations in comparison with surrounding structures. These features were emphasized in Figures 11(d), 11(e), and 11(f), which were obtained by zooming in on the square areas bounded by the white dotted lines in Figure 11(a), 11(b), and 11(c), respectively. While the noncontact image appeared relatively smooth over the entire zoomed area as shown in Figure 11(d), the surface was rougher in the contact regimes in their respective areas (Figure 11(e) and Figure 11(f)). For example, the enclosed area with the dashed boundary was more protruded in the contact regime than in the noncontact regime. In the same contact regimes, some areas show the contrast reversals, depending on the polarity of applied forces. For example, the area encircled with the dotted white boundary showed elevated height for the positive applied force and compressed depth for the negative applied force. An area bounded with the solid line showed a compression when the applied force is positive, whereas it showed a stretching when the applied force was negative.

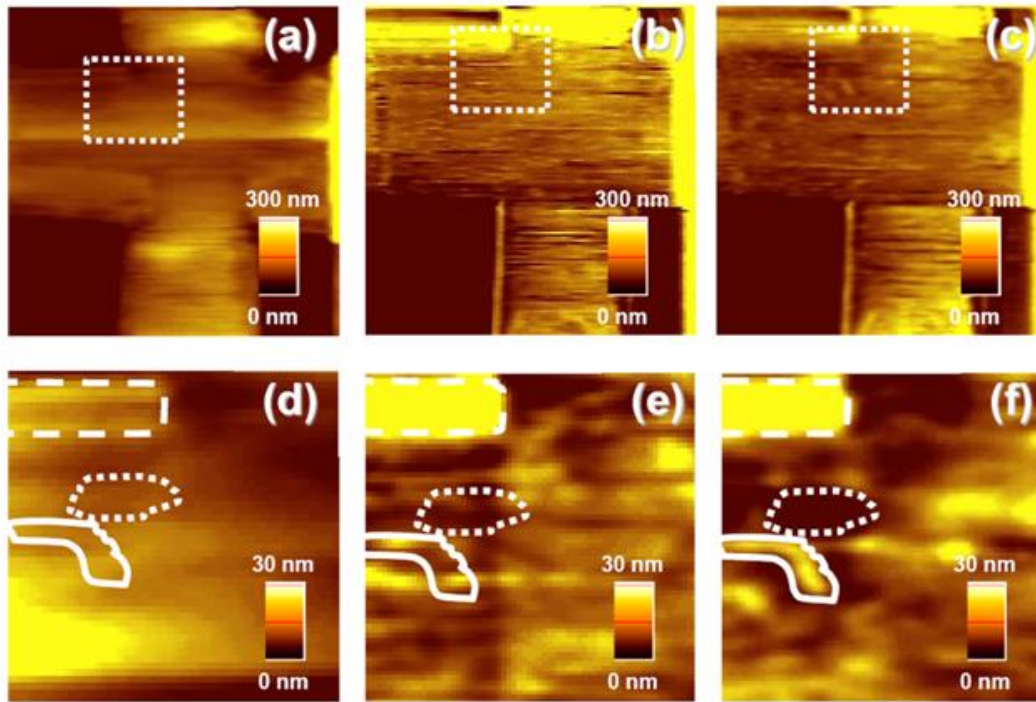


Figure 11. Constant-force image collected with a scan size of $5 \mu\text{m} \times 5 \mu\text{m}$ on the grating structure at an imaging rate of 0.08 frames per second at (a) 1.25 nN set-force under normal polarity, (b) 1.25 nN set-force under reversed polarity, and (c) -1.25 nN set-force under reverse polarity. The square area with white dashed lines is zoomed in and displayed as (d) for the normal polarity 1.25 nN set-force image, (e) for the reversed polarity 1.25 nN set-force image, and (f) for the normal polarity -1.25 nN set-force image. The dashed boundary and the dotted boundary encircle areas considered as representative areas having high spring constant, while the solid boundary encircles an area representative of having a low spring constant.

The local contrast difference, dependent on the polarity of the applied set-force, suggested that some materials embedded in adsorbed material have different mechanical properties, such as elastic modulus from surrounding materials [24]. The mechanical difference led to the varying compression depth and stretching height, creating images dependent on the polarity of the set-force. This embedded material was modeled with a weak spring surrounded with two strong springs with different heights that represent the corrugated surrounding materials, as shown in Figures 12(a), 12(b), and 12(c). During the noncontact imaging, the tip follows the trace of the topographic structure, as drawn with a dashed line in Figure 12(a).

It is important to note that the topographical contributions by electrostatic and van der Waals forces were negligible. The electrostatic and van der Waals forces were estimated to be about $\sim 0.003 \text{ nN}$ and $\sim 0.001 \text{ nN}$, respectively, at the distance of 27 nm where the noncontact imaging was performed. In this estimation, we used the tip radius of 10 nm, Hamaker constant of $3 \times 10^{-19} \text{ J}$ [91], and an assumed surface potential of $\sim 400 \text{ mV}$ found for a polar polymer, z-dol perfluoropolyether [92]. Using the sample spring constant of $\sim 1 \text{ N/m}$ found above, the electrostatic and van der Waals forces only contribute $\sim 3 \text{ pm}$ and $\sim 1 \text{ pm}$, respectively.

In the repulsive-contact regime the applied force was positive (as seen in Figure 12(b)), thus the soft spring was compressed more than the surrounding stiff springs, creating a larger degree of compression depth at the soft spring in the constant-force images [24]. As shown in the trace marked with a dashed line, it was more corrugated than the trace in the noncontact regime. When the imaging was performed in the attractive-contact regime, the applied force was negative (as shown in Figure 12(c)); therefore, the weak spring was stretched more than the surrounding stiff springs, creating a substantial protruding feature in the constant-force image. Again, the corrugation is higher than the trace of noncontact mode image, but it was similar to that obtained in the repulsive contact regime. This model explained the observed roughness difference between noncontact and contact images, as seen in Figures 11(a), 11(b) and 11(c). Additionally, it explained the contrast variation dependent on the polarity of the applied force during contact mode imaging. This model suggested that the force-feedback HSAFM system is capable of differentiating a local area with a different spring constant from that of the surrounding material by comparing the repulsive-contact and attractive-contact images. The effect of varying thicknesses and porosity of the film on its observed structural and mechanical properties could be an interesting future topic.

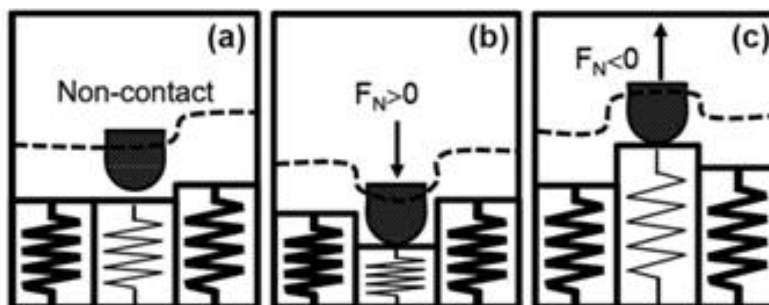


Figure 12. Diagrams of spring-like behavior when imaging in the (a) attractive-noncontact regime, (b) repulsive-contact regime, and (c) attractive-contact regime. The dashed lines represent the sectional profile taken over the surface at the constant force modes.

6. IMAGING STABILITY

The force-feedback HSAFM was then further applied to the high-speed imaging of a soft hydrocarbon film with large topographic height variations to investigate the stability of the system [27]. As stability information was largely lacking for the force-feedback HSAFM, this investigation was vital to further understanding the limitations of the newly created system, and thus providing insight into avenues upon which the system would be able to be enhanced. The influence of the applied loading force, hydrophilicity, and imaging rate on image stability of the system was investigated by comparing both interfacial force spectroscopic and topographic information. First, force-distance curves were collected on the grating sample covered by the adsorbed material film. As expected, both approach (Figure 13(a)) and retraction (Figure 13(b)) curves do not show any snap-to-contact phenomenon due to the zero compliance effect during the force-distance measurement. The data show that the minimum force is -1.5 nN on approach, while the minimum force is -2 nN on retraction.

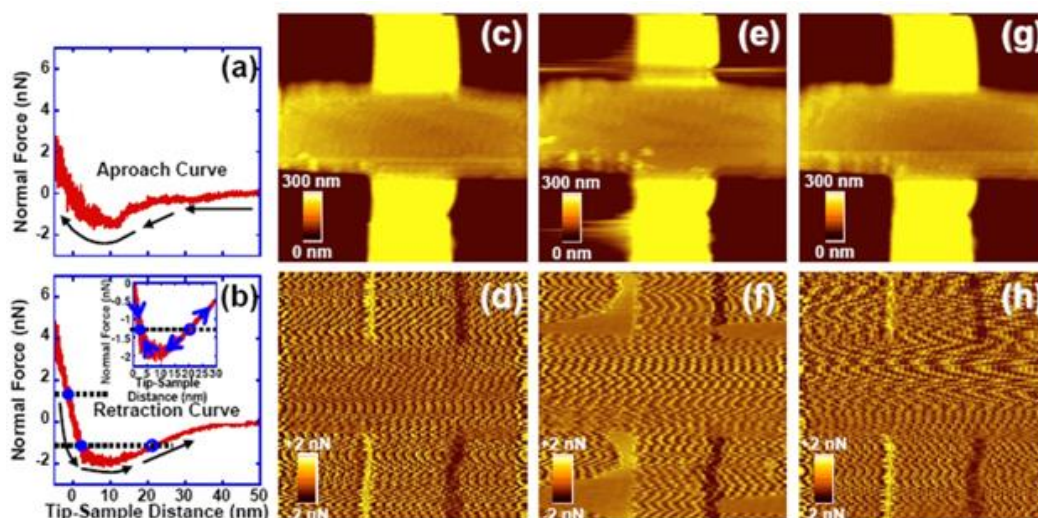


Figure 13. Force-distance curve between the tip and a two-dimensional grating structure with $10\ \mu\text{m}$ periodicity, with a force-activated voltage-feedback system during approach (a) and retraction (b). Dotted lines represent the applied force values, where the closed circles represent intersection of the curve with negative slope and the open circle represents the intersection of the curve with positive slope. (Inset) a zoomed-in view of the force distance curve at the negative-positive slope transition point. The arrows in the inset show the direction in which the feedback moves from imaging states. The imaging states are marked by the closed and open circle on the dotted line. Constant-force topographic (c,e,g) and simultaneous force (d,f,h) images collected in a scan size of $10\ \mu\text{m} \times 10\ \mu\text{m}$ on the grating structure at an imaging rate of 0.1 frames per second at applied-forces of $+1.25\ \text{nN}$ (a, b), $-1.25\ \text{nN}$ (c,d), $+1.25\ \text{nN}$ (e,f).

The displayed minute attractive force encountered on approach (as seen in Figure 13(a)) implies that the outer surface of the adsorbed material was hydrophobic in nature, consistent with our earlier report [24]. The hydrophobicity of the surfaces was derived from the nonpolar hydrophobic surface, which prefers to orient outward to be exposed to ambient air molecules which are predominantly nonpolar. The stiffness of the sample was found to be $\sim 0.77\ \text{N/m}$ from a linear curve fitting made in the repulsive regime from $-5\ \text{nm}$ to $2\ \text{nm}$ tip-sample distance in Figure 13(b).

As seen in Figure 13(b), when imaging with a positive applied force (indicated by a dotted line representing the applied-force of $+1.25\ \text{nN}$), there was only one stable imaging condition: the intersection of the dotted line and the force-distance curve, represented by a solid circle [27]. However, when imaging with a negative applied force, there was one stable and one unstable imaging conditions indicated by the solid circle and open circle, respectively, on the dotted line at $-1.25\ \text{nN}$. We hypothesized that when imaging the grating sample, as the tip reached the sudden height deviation associated with the step structure, the tip-sample distance would momentarily increase, which would cause a negative rise in force in the force-distance curve. This negative rise could potentially trigger a shift from the negative sloped stable imaging condition (closed circle) to the positive sloped unstable imaging condition (open circle), thus causing imaging instability as the tip transitioned between the two imaging states. When encountering a large topographic variation, the tip-sample distance change will cause the feedback of the system to adjust the tip-sample

distance in such a manner as it perceives will bring the system back to the set-force imaging condition (as depicted by the inset of Figure 13(b)). However, if the system is pushed past the unstable imaging point (open circle), the system will reset and attempt to increase the tip-sample distance in order to increase force as if it were near the stable imaging condition. This causes the feedback to move in the wrong direction (as in the direction of the right most arrow), creating an unstable imaging condition. At -1.25 nN set-force, because only a slight amount of force ~ 0.75 nN is needed to make the transition between the two states, the feedback perturbation (i.e., the sudden tip-sample distance change) should allow for switching between the imaging states at almost equal probability during the data acquisition near the step-structures of the grating sample.

To test this hypothesis, a sequence of high-speed imaging with different loading forces was performed [27]. Figures 13(c) and 13(d) show a topographic and force image taken at a high-speed imaging rate of 0.1 frames per second with a set force of +1.25 nN. The force image (as seen in Figure 13(d)) is shown to remain relatively constant except when encountering areas that contain abruptly changing large structures (such as the grating steps). Since the force-feedback scheme controls the cantilever compliancy to make the deflection of the cantilever zero, the observed force changes were due to the limited response time of the current force-feedback system to the sudden force changes. Therefore, through this relatively constant applied force, the topographic image could be regarded as a constant-force image. The topographic image showed many rounded features (presumably dust) with diameters of 10-300 nm that had accumulated on the grating structure during the long storage period in air. To raise the tip above the adsorbed material, the applied force was changed from positive to negative. Figures 13(e) and 13(f) show a topographic and force image, respectively, with some streaky fringe structures that flow in the scan direction. These streaky features represent moments of imaging instability after the system encountered a relatively large jump in tip-sample distance. The system was able to recover relatively quickly depending on how far off the stable imaging set-point (as indicated by the solid circle in the inset of Figure 13(b)) the imaging condition was moved. When the applied force was changed back to the positive value, those streaky structures disappeared (as seen in Figures 13(g) and 13(h)). The appearance of the streaky structures when imaging at -1.25 nN set force, and then the disappearance when imaging at +1.25 nN set force, confirmed the hypothesis that the negative set-point value would allow for transition between the two imaging states, depending on tip-sample distance (as seen in Figure 13(b)), and verified that the tip did not pick up any material.

The grating structure then underwent a strict cleaning procedure (described in the Materials and Methods section) to remove the adsorbed material layer in order to obtain a comparison with the underlying known, hard hydrophilic grating structure [27]. Force-distant graphs were compiled for the approach (Figure 14(a)) and retraction (Figure 14(b)) process. The data showed that on approach the minimum attractive force is -39 nN while on retraction the minimum attractive force is -75.5 nN. The slight hysteresis between the two minima may have indicated the possible involvement of bonding formation and rupture of residual hydrocarbons in interactions between two surfaces at the molecular scale. When compared to the previous attractive forces of the unclean sample, the forces increased by a factor of more than ten.

The increase in attractive forces indicated that water meniscus formed between the hydrophilic sample surface and the tip due to the removal of the hydrophobic components

observed in Figure 13(c). Interestingly, a periodic feature appeared between 0 nm and 8 nm during the approach process, denoted as P1 and P2 in Figure 14(a) [27]. The periodicity was calculated to be ~ 3 nm, possibly suggesting distance-dependent structural transition [16, 17] of the water meniscus. In contrast, the periodic feature was absent in the force-distance curve on retraction. To verify the hardness of the sample, a linear curve fitting was made from -1.1 nm to 0.4 nm tip-sample distance in Figure 14(b), thus giving a spring constant of ~ 57 N/m. Therefore, the spring constant is shown to be much larger than the 0.77 N/m observed in Figure 13(b). Additionally, because a much larger negative force of ~ 70 nN than the ~ 0.75 nN of Figure 13(b) was needed to make the transition between the two imaging conditions (as seen in Figure 14(b)), even when the distance between the stable and unstable imaging states was only ~ 2 nm, it could be anticipated that with a set force of -1.25 nN, the probability of reaching the unstable imaging condition was minute. To test this hypothesis and to verify the sample's cleanliness, a topographic image was taken with a scan area of $8 \mu\text{m} \times 8 \mu\text{m}$, at the same set force value of -1.25 nN, and at the same high imaging rate of 1.7 frames per second. The high-speed topographic image in Figure 14(c) does not show the same features related to the hydrocarbon film observed in Figure 13(c). This result verified the sample's cleanliness and indicates that the hypothesis was valid in that under the current circumstances, the system did not reach the unstable imaging condition even when encountering the large topographic step heights of the grating sample. This result suggested that the imaging stability is dependent on the strength of adhesion between the tip and the surface.

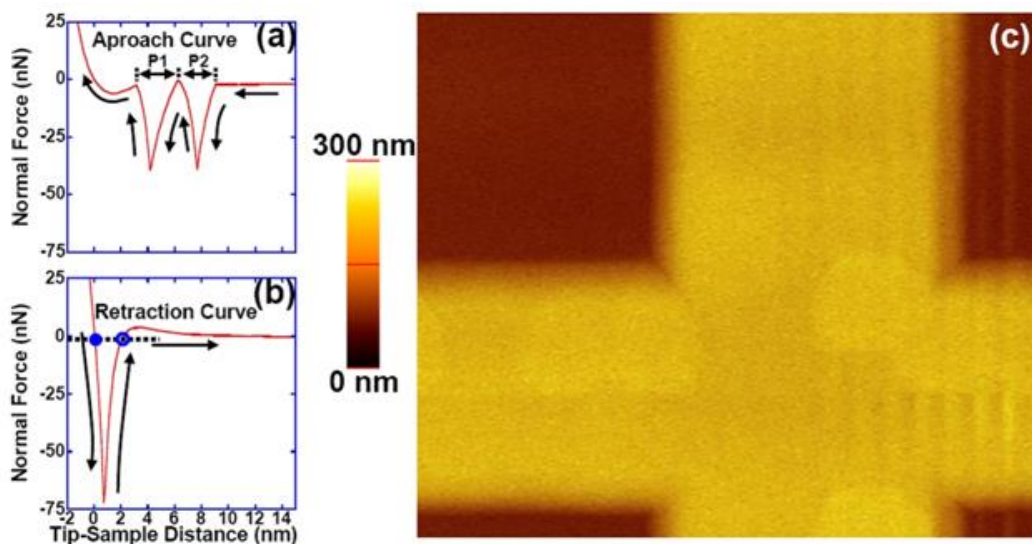


Figure 14. Force-distance curves measured without lateral modulation at RH 30% during approach (a) and retraction (b). P1 and P2 represent the period of oscillation. The segment after P2 is the transitional interval from oscillatory to repulsive force by the sample surface. The dashed line represents the imaging applied-force value; the closed circles represent the intersection of the curve with negative slope; the open circle represents the intersection of the curve with positive slope. (c) Fast topographical images collected at -1.25 nN force set in a scan size of $8 \mu\text{m} \times 8 \mu\text{m}$ on the cleaned grating structure at an imaging rate of 1.7 frames per second.

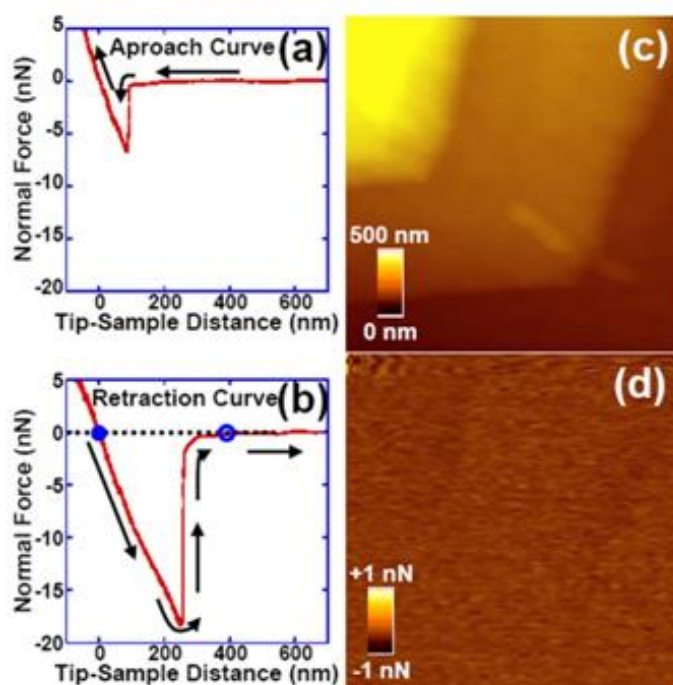


Figure 15. Force-distance curve between the tip and an *E. coli* sample, with a force-activated voltage-feedback system during approach (a) and retraction (b). The dashed line represents the imaging applied-force value; where the closed circles represent intersection of the curve with negative slope and the open circle represent intersection of the curve with positive slope. Topographical and force images collected simultaneously at 0 nN set-force on *E. coli* biofilm with a planktonic cell at ~ 0.008 frames per second (c, d). The scan area is $8 \mu\text{m} \times 8 \mu\text{m}$ with 128×128 data points.

Now that the effects of the applied force on the imaging condition were known, attention was focused on the effects derived from the imaging rate [27]. In this regard, real-world biological applications were tested by using a very soft *E. coli* sample. The force-distance approach curve (Figure 15(a)) showed that initially the tip did not experience any force until the tip came in contact with the biomaterial. On approach, the tip experienced a sudden attractive force of -6.5 nN due to the tip contact with the material surface (seen to be approximately 95 nm from the force-distance curve). The tip force then increased linearly as the tip-substrate distance decreased, causing the tip to push against the biomaterial. When the tip retracted (Figure 15(b)), the linear force followed the original approaching curves, indicating that the observed force was similar to a reversible process. However, below the tip distance of zero, the adhesive force linearly continued until it reached 245 nm . At 245 nm , the attractive force rapidly increased toward zero and then slowed down near zero. The relatively large pull-off force (18 nN), in comparison to the attractive force (6.5 nN) on approach in the force-distance curve, indicated the existence of adhesive bonding between the tip and the biomaterial. As the distance increased after the breakage of the adhesive bonding, van der Waals forces and electrostatic interactions were the only contributions to the observed attraction at the distance larger than 26 nm . Interestingly, the linear dependence of the force on the distance suggested that the adhesive internal material behaved like a linear spring that follows Hooke's law. A linear curve fitting from -63 nm to 226 nm tip-sample distance in

Figure 15(b) provided a spring constant value of 0.076 N/m, a fractionally smaller value than seen in the soft hydrocarbon film in Figure 13(b). At the standard operating applied force of 0 nN, where the distance was ~320 nm apart between the two imaging conditions along with the relatively large pull-off force of 18 nN, the chance that the unstable imaging condition would be reached was highly improbable. As before, to confirm this hypothesis, topographic and force images were collected of biofilms with a single cell of *E. coli* on the grating sample under varying imaging rates.

Figure 15(c) shows an 8 μm x 8 μm high resolution topographic image and Figure 15(d) shows the corresponding force image, taken at a rate of ~0.008 frames per second, of what appears to be a sequence of step-like biofilm structures (with each step height of ~200 nm) developed during the sample preparation. The image contains a small rod shape about 2-3 μm long and about 0.5 μm in diameter in the lower right corner. The structure was considered a lone *E. coli* cell because the dimension and morphology was consistent with the literature values of *E. coli* [28]. The *E. coli* was shown to have the characteristic smooth texture for the cell surface with a small indentation in the center of the cell. 0 nN applied force was an ideal imaging condition for biological specimens as it is not invasive, as seen in Figure 15(c), with the tip following topographic features faithfully [22]. The force image (Figure 15(d)) was virtually constant as a result of the slow scan rate that allowed for the piezo tube feedback to compensate for all topographic signals.

Nonetheless, when the imaging rate was accelerated, the force image became rougher due to the limiting capability of the piezo tube's response to the rapid signal change [27]. The high-resolution topographic imaging was not degraded at all as the rate was increased from ~0.008 frames per second to ~1 frame per second. Figures 16(a) and 16(b), respectively, show the high-speed topographic and force images collected simultaneously at the same location at an imaging rate of ~1 frame per second. The force images show that the force was constant on the upper terrace of the grating except when abrupt signal changes occur due to small features. The high-speed force image (Figure 16(b)), compared to the high-speed topographic image, shows better contrast, which could be used as complementary information in understanding the delicate structural changes on the biological surfaces. This higher contrast was due to the residual force signals that were not compensated by the topographic feedback loop when abrupt changes occurred in the sample's mechanical property or topography. The high-speed force images were analogous to frictional images in friction force microscopy [53, 54] where the sample's boundaries were always emphasized. For example, those delicate features in the high-speed force image cannot be easily identified with the topographic image only. A small y-axis striation pattern started to appear as the rate was increased from ~1 frame per second to 2 frames per second. The pattern increased in intensity from the left to the right side in the high-speed topographic image (Figure 16(c)) and was particularly prominent in the high-speed force image (Figure 16(d)). The striation pattern has been observed previously and found to be due to the piezo tube approaching resonant vibration frequency (e.g., [1, 4, 55-57]). The fastest observed scan rate possible, without experiencing any effect from the resonance frequency, was approximately 1 frame per second. This was roughly consistent with our previous observation, where the imaging rate was found to be limited by the resonance frequency of the piezo tube [22]. When increasing the rate from 2 frames per second to 5 frames per second, the patterns were shown to become more dominant as the scan rate increased. The high-speed topographic and force images taken with the scan

rate of 5 frames per second can be seen as Figure 16(e) and Figure 16(f), respectively. Both images show a larger striation pattern parallel to the y-axis. Due to the cooperativeness between the force-feedback loop and the piezo tube feedback loop, the system was able to capture distinguishable biological features at roughly 5 frames per second for an image with scan area $8\ \mu\text{m} \times 8\ \mu\text{m}$, an acquisition rate 600-1000 times faster than conventional AFMs [94].

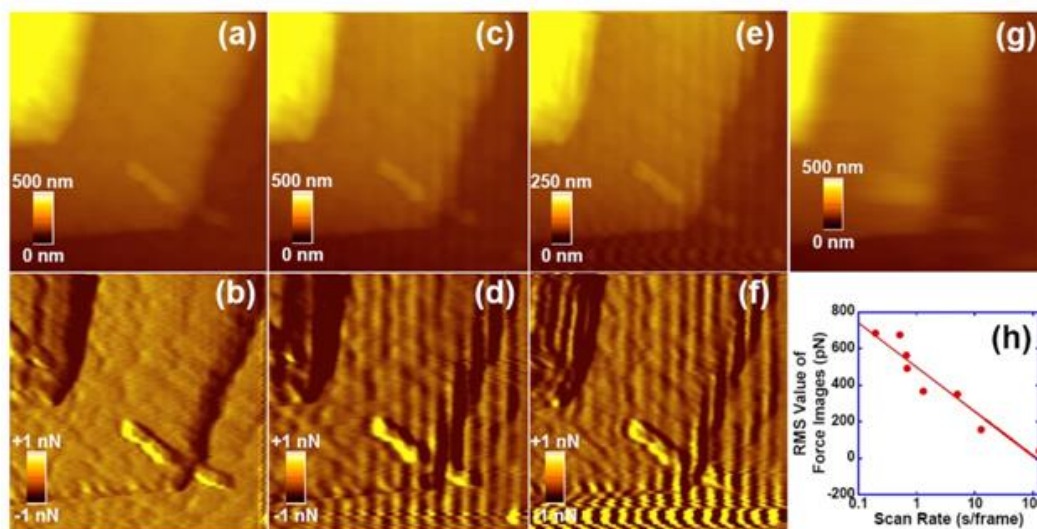


Figure 16. Topographical and force images collected simultaneously at 0 nN set-force on *E. coli* biofilm with a planktonic cell at three different scan rates: 1 frame per second (a, b), 2 frames per second (c, d), 5 frames per second (e, f). An additional topographic image is shown for ~ 10 frames per second (g). The scan area is $8\ \mu\text{m} \times 8\ \mu\text{m}$ with 128×128 data points. RMS value vs. scan rate plot for force images in logarithmic scale (h).

When the imaging rate was increased to 10 frames per second (Figure 16(g)), the RHK controller was unable to record high-speed topographic and force images at the same time [27]. The high-speed topographic image shows that the topographic features became too distorted to be accurately distinguishable. This result indicated that the HSAFM imaging speed was limited to 5 frames per second, which was consistent with response time of the DMASP cantilever [22]. Although, when the signal variation was faster than the time resolution of the system, those features appeared as an error signal rather than a topographic signal. This was supported by the fact that when imaging at the rate of 10 frames per second (see Figure 16(g)), the image displayed less defined small features in the topographic images because the signal was too fast for the system to respond when the imaging rate was above 5 frames per second. However, it was important to distinguish these low-resolution features related to the signal variation as being faster than the time resolution of the system from those features associated with the unstable imaging condition (as seen in Figure 13(e)). This was verified by the fact that the 10 frames per second image in Figure 16(g) still shows appreciably large topographic features. Therefore, under the capable imaging rates of the system, it was found that the imaging rate does not influence stable and unstable imaging transitions.

The RMS values of force images were plotted as a function of scan rates in logarithmic scale (Figure 16(h)) [27]. The plot exhibited an exponential decay curve pattern. The RMS values resulted from the tip oscillating while scanning at high speeds near the resonance frequency, thus inducing a minute oscillatory force. While the system experienced an oscillatory force of ~ 0.039 nN in RMS value at the imaging speed of ~ 0.008 frames per second, it experienced an increased oscillatory force of ~ 0.5 nN in RMS value at the imaging speed of 5 frames per second. However, this small force was not nearly enough to push the imaging to the unstable imaging state as the minimum of the curve was at 17 nN. As no notable changes were discernible in the *E. coli* shape and the biofilm steps except for the striation artifacts in the series of HSAFM images, the gram-negative cell seemed to have sufficient tensile strength in its cell walls that it was not damaged by the oscillatory forces, even though the tip was in contact with the sample. Although, if the sample had been more delicate and had less tensile strength (such as a mammalian cell), then the imaging rate would likely need to have been decreased in order for the system to avoid the oscillatory force and therefore be less invasive. The proof of concept of the force-feedback HSAFM was substantiated through the high-speed imaging of large biological samples on the micro level rather than the conventional nano-level, enabling high-speed imaging at a multiple-cellular level [22]. To verify the system's ability to measure mechanical properties it was confirmed that the spring of the cantilever could be negated and the spring constant of the surface was able to be isolated [24].

CONCLUSION

We designed and developed a force-feedback HSAFM for imaging large-scale biological samples, which solved the issues related to the use of a smaller cantilever, increasing the AFM imaging speed through a self-actuation cantilever that is capable of fast response through a force-feedback mechanism. The force-feedback shortens the response time of the sensor, which is the most essential component for HSAFM. Three different images, a deflection image, a topographic image, and a force image, were collected simultaneously to have complementary information in biological studies. We demonstrated that the force-feedback HSAFM is capable of imaging *E. coli* and related biofilms at an imaging rate of 5 frames per second.

The force-feedback HSAFM is also capable of identifying buried nanoscale structures embedded in soft samples. The system performs the constant-force imaging of the film in both contact and noncontact regimes, which is not possible with the conventional AFM system. Both constant-force images taken in the repulsive and attractive contact regimes revealed additional features that were not observed in the images taken in the noncontact regime. Interestingly, some contrast reversal features were observed between the two contact regimes, while the average roughness remained constant. The contrast change was explained by modeling the adsorbed materials and embedded impurities with simple springs with different spring constants. These results suggest that the force-feedback HSAFM technique can be applied to biological materials including DNA and many industrial processes where the mechanical and structural properties and their relationship are critical. In chemical-mechanical planarization (CMP) processes and microelectromechanical systems (MEMS), for

example, the in-depth understanding of the indentation depth under constant and varying load forces and the understanding of structure of buried materials are important. The combination of the force-feedback HSAFM with other optical methodology (e.g., Raman spectroscopy or infrared spectroscopy) will provide more opportunity to understand the mechanical and structural properties of soft materials in relation to chemical composition.

The imaging stability in force-feedback HSAFM is dependent on the applied loading force, hydrophilicity, and imaging rate. We collected force-distance curves, topographic and force information for a variety of samples and parameters. When the force-distance curves were correlated with the images of an ambient adsorbed hydrophobic material layer on a grating sample with large step structures, we found that stable and unstable imaging conditions depend on the distance between two points that satisfy the applied-force value in the force-distance curve. When the sample adhesional property was changed from hydrophobic to hydrophilic by cleaning the surface of silicon grating, the enhanced adhesion between the tip and the surface improved the imaging stability. When we tested the influence of the imaging rate on imaging stability of an *E. coli* biofilm and planktonic cell, imaging was stable even at the high-speed imaging rate of 5 frames per second. Therefore, it can be concluded that the transitions between stable and unstable imaging conditions rely on applied force and hydrophilicity of the sample, but is independent of imaging rates up to the tested maximum rate of 10 frames per second. With the cooperative use of these variables that influence imaging stability, force-feedback HSAFM will potentially contribute to the imaging and understanding of hard and soft materials, including a vast variety of biological systems.

REFERENCES

- [1] Ando, T.; Kodera, T.; Takai, E.; Maruyama, D.; Saito, K.; Toda, A. *Proc. Natl. Acad. USA*, 2001, 98, 12468-12472.
- [2] Crampton, N.; Yokokawa, M.; Dryden, D. T. F.; Edwardson, J. M.; Rao, D. N.; Takeyasu, K.; Yoshimura, S. H.; Henderson, R. M. *Proc. Natl. Acad. USA*, 2007, 104, 12755-12760.
- [3] van Noort, S.J, van Der Werf, K. O.; de Grooth, B. G.; Greve, J. *Biophys J.*, 1999, 77, 2295-2303.
- [4] Ando, T.; Uchihashi, T.; Fukuma, T. *Prog. Surf. Sci.*, 2008, 83, 337-437.
- [5] Ando, T.; Uchihashi, T.; Kodera, N.; Yamamoto, D.; Taniguchi, M.; Miyagi, A.; Yamashita, H. *Pflügers Archiv - Eur. J. Physiol.*, 2008, 456, 211-225.
- [6] Viani, M. B.; Schaffer, T. E.; Paloczi, G. T.; Pietrasanta, I.; Smith, B. L.; Thompson, J. B.; Richter, M.; Rief, M.; Gaub, H. E.; Plaxco, K. W.; Cleland, A. N.; Hansma, H. G.; Hansma, P. K. *Rev. Sci. Instrum.*, 1999, 70, 4300-4303.
- [7] Humphris, A. D. L, Miles, M. J.; Hobbs, J. K. *Appl. Phys. Lett.*, 2005, 86, 034106.
- [8] Kodera, N.; Sakashita, M.; Ando, T. *Rev. Sci. Instrum.*, 2006, 77, 083704.
- [9] Picco, L. M.; Bozec, L.; Ulcinas, A.; Engledew, D. J.; Antognozzi, M.; Horton, M. A.; Miles, M. J. *Nanotechnology*, 2007, 18, 044030-044033.
- [10] Zou, Q.; Leang, K. K.; Sadoun, E.; Reed, M. J.; Devasia, S. *Asian J. Control.*, 2008, 6, 164-178.

-
- [11] Fantner, G. E.; Barbero, R. J.; Gray, D. S.; Belcher, A. M. *Nat. Nanotechnol.*, 2010, 5, 280–285.
- [12] Hansma, P. K.; Schitter, G.; Fantner, G.E.; Prater, C. *Science*, 2006, 314, 601-602.
- [13] Katan, A. J.; Dekker, C. *Cell*, 2011, 147, 979-982.
- [14] Walters, D. A.; Cleveland, J. P.; Thomson, N.; Hansma, P. K.; Wendman, M.; Gurley, G.; Elings, V. B. *Rev. Sci. Instrum.*, 1996, 67, 3583–3590.
- [15] Bonander, J. R.; Kim, B. I. *Appl. Phys. Lett.*, 2008, 92, 103124.
- [16] Kim, B. I.; Bonander, J. R.; Rasmussen, J. A. *Rev. Sci. Instrum.*, 2011, 82, 053711.
- [17] Kim, B. I.; Rasmussen, J. A.; Kim, E. J. *Appl. Phys. Lett.*, 2011, 99, 201902.
- [18] Aimé, J. P.; Elkaakour, Z.; Odin, C.; Bouhacina, T.; Michel, D.; Curély, J. ; Dautant, A. *J. Appl. Phys.*, 1994, 76, 754-762.
- [19] Burnham, N. A.; Colton, R. J. *J. Vac. Sci. Technol. A.*, 1989, 7, 2906-2913.
- [20] Lodge, K. B. *Adv. Coll. Interface Sci.*, 1983, 19, 27-73.
- [21] Meyer, E.; Heinzelmann, H.; Grütter, P.; Jung, T. H.; Weisskopf, T.; Hidber, H. R. Lapka, R.; Rudin, H.; Güntherodt, H. J. *J. Microsc.-Oxford*, 1988, 152, 269-280.
- [22] Kim, B. I.; Boehm, R. D. *Micron*, 2012, 43, 1372-1379.
- [23] Reprinted from *Scanning*, 35, B. I. Kim and R. D. Boehm, Mechanical Property Investigation of Soft Materials by Soft Materials by Cantilever-Based Optical Interfacial Force Microscopy, 59-67, 2013, with permission from Elsevier.
- [24] Kim, B. I.; Boehm, R. D. *Scanning*, 2013, 35, 59-67.
- [25] Radmacher, M.; Tillmann, RW.; Fritz, M.; Gaub HE. *Science*, 1992, 257, 1900-1905.
- [26] Mate, C. M. *Tribology on the Small Scale: A Bottom up Approach to Friction, Lubrication, and Wear*; Oxford Univ. Press.: New York, NY, 2008.
- [27] Kim, B. I.; Boehm, R. D. *Ultramicroscopy*, 2013, 125, 29-34.
- [28] Alberts, B.; Johnson, A.; Lewis, J.; Raff, M.; Roberts, K.; Walter, P. *Molecular Biology of The Cell*, fourth ed; Garland Science: New York, NY, 2002.
- [29] Sulchek, T.; Hsieh, R.; Adams, J. D.; Yaralioglu, G. G.; Minne, S. C.; Quate, C. F.; Cleveland, J. P.; Atalar, A.; Adderton, D. M. *Appl. Phys. Lett.*, 2000, 76, 1473-1475.
- [30] Kühle, A.; Sørensen, A. H.; Bohr, J. *J. Appl. Phys.*, 1997, 81, 6562–6569.
- [31] Garcia, R.; San Paulo, A. *Phys. Rev. B* 2000, 61, R13381-R13384.
- [32] Henze, T.; Schröter, K.; Thurn-Albrecht, T. *Nanotechnology*, 2012, 23, 245702.
- [33] Santos, S.; Barcons, V.; Font, J.; Thomson, N. H. *Nanotechnology*, 2010, 21, 225710.
- [34] Kim, B. I. *Rev. Sci. Instrum.*, 2009, 80, 023702.
- [35] Joyce, S. A.; Houston, J. E. *Rev. Sci. Instrum.*, 1991, 62, 710-715.
- [36] Reprinted from *Micron*, 43, B. I. Kim and R. D. Boehm, Force-Feedback High-Speed Atomic Force Microscope for Studying Large Biological Systems, 1372-1379, 2012, with permission from John Wiley and Sons.
- [37] Veeco. Probes and Accessories. Veeco: Santa Barbara, CA, 2006.
- [38] Manalis, S. R.; Minne, S. C.; Quate, C. F. *Appl. Phys. Lett.*, 1996, 68, 871-873.
- [39] Manalis, S. R.; Minne, S. C.; Atalar, A.; Quate, C. F. *Rev. Sci. Instrum.*, 1996, 67, 3294-3297.
- [40] Minne, S. C.; Manalis, S. R.; Quate, C. F. *Appl. Phys. Lett.*, 1995, 67, 3918-3920.
- [41] Rogers, B.; York, D.; Whisman, N.; Jones, M.; Murray, K.; Adams, J. D.; Sulchek, T.; Minne, S. C. *Rev. Sci. Instrum.*, 2002, 73, 3242-3244.

-
- [42] Rogers, B.; Sulchek, T.; Murray, K.; York, D.; Jones, M.; Manning, L.; Malekos, S.; Beneschott, B.; Adams, J. D.; Cavazos, H.; Minne, S. C. *Rev. Sci. Instrum.*, 2003, 74, 4683-4686.
- [43] Sulchek, T.; Minne, S. C.; Adams, J. D.; Fletcher, D. A.; Atalar, A.; Quate, C. F.; Adderon, D. M. *Appl. Phys. Lett.*, 1999, 75, 1637-1639.
- [44] Oulevey F.; Gremaud G.; Sémoroz A.; Kulik A. J.; Burnham N. A.; Dupas E.; Gourdon D. *Rev. Sci. Instrum.*, 1998, 69, 2085-2094.
- [45] Ashurst W. R.; Carraro C.; Maboudian R. *IEEE Trans. Device Mater. Rel.*, 2003, 3, 173-178.
- [46] Cabuz C. C.; Cabuz E. I.; Ohnstein T. R.; Neus J.; Maboudian R. *Sens. Actuators, A*, 2000, 79, 245-250.
- [47] de Boer M. P.; Michalske T. A. *Mater. Res. Soc. Symp. Proc.*, 1997, 444, 87-92.
- [48] de Boer M. P.; Knapp J. A.; Redmond J. M.; Michalske T. A. *Mater. Res. Soc. Proc.*, 1998, 518, 131-136.
- [49] de Boer M. P.; Knapp J. A.; Mayer T. M.; Michalske T. A. *Proc. SPIE*, 1999, 3825, 2-15.
- [50] Maboudian R. *Surf. Sci. Rep.*, 1998, 30, 207-269.
- [51] Tanner D. M.; Walraven J. A.; Irwin L. W.; Dugger M. T.; Smith N. F.; Eaton W. P.; Miller W. M.; Miller S. L. *Proc. IEEE Intern. Rel. Phys. Symp.*, 1999, 189-197.
- [52] Zhao Y. P.; Wang L. S.; Yu T. X. *J. Adhesion Sci. Technol.*, 2003, 17, 519-546.
- [53] Baselt D. R.; Baldeschwieler J. D. *J. Appl. Phys.*, 1994, 76, 33-38.
- [54] Overney R. M.; Bonner T.; Meyer E.; Ruöetschi M.; Luöthi R.; Howald L.; Frommer J.; Guötherodt H. J.; Fujihira M.; Takano H. *J. Vac. Sci. Technol.*, 1994, 12, 1973-1976.
- [55] Miyagi, A.; Tsunaka, Y.; Uchihashi, T.; Mayanagi, K.; Hirose, S.; Morikawa, K.; Ando, T. *Chem. Phys. Chem.*, 2008, 9, 1859-1866
- [56] Schitter, G.; Menold, P.; Knapp, H.; Allgöwer, F.; Stemmer, A. *Rev. Sci. Instrum.*, 2001, 72, 3320-3931.
- [57] Sparks A. W.; Manalis, S. R. *Appl. Phys. Lett.*, 2004, 85, 3929-3931.
- [58] Allison, D. G. *Community structure and co-operation in biofilms*; Cambridge University Press: Cambridge, UK, 2000.
- [59] Lynch, J. F.; Lappin-Scott, H. M.; Costerton, J. W. *Microbial biofilms*; Cambridge University Press: Cambridge, UK, 2003.
- [60] Dufrière, Y. F. *Nat. Rev. Microbiol.*, 2004, 2, 451-460.
- [61] Zareian Jahromi, S. A.; Salomons, M.; Sun, Q.; Wolkow, R. A. *Rev. Sci. Instrum.*, 2008, 79, 076104.
- [62] Rost, M. J.; van Baarle, G. J. C.; Katan, A. J.; van Spengen, W. M.; Schakel, P.; van Loo, W. A.; Oosterkamp, T. H.; Frenken, J. W. M. *Asian. J. Control.*, 2009, 11, 110-129.
- [63] Akari, S. O.; van der Vegte E. W.; Grim P. C. M.; Belder G. F.; Koutsos V.; ten Brinke G.; Hadziioannou G. *Appl. Phys. Lett.*, 1994, 65, 1915-1917.
- [64] Bhushan B.; Koinkar V. N. *Appl. Phys. Lett.*, 1994, 64, 1653-1655.
- [65] Burnham N. A.; Gremaud G.; Kulik A. J.; Gallo P. J.; Oulevey F. *J. Vac. Sci. Technol. B*, 1996, 14, 1308-1312.
- [66] Fretigny C.; Basire C.; Granier V. *J. Appl. Phys.*, 1997, 82, 43-48.
- [67] Burnham N. A. *J. Vac. Sci. Technol. B*, 1994, 12, 2219-2221.

-
- [68] Cappella B.; Baschieri P.; Frediani C.; Miccoli P.; Ascoli C. *Nanotechnology*, 1997, 8, 82-87.
- [69] Heuberger M.; Dietler G.; Schlapbach L. *Nanotechnology*, 1994, 5, 12-23.
- [70] Hosaka S.; Koyanagi H.; Kikukawa A.; Miyamoto M.; Nakamura K.; Etoh K. *J. Vac. Sci. Technol. B*, 1997, 15, 788-792.
- [71] Maivald P.; Butt H. J.; Gould S. A. C.; Prater C. B.; Drake B.; Gurley J. A.; Elings V. B.; Hansma P. K. *Nanotechnology*, 1991, 2, 103-106.
- [72] Miyatani T.; Horii M.; Rosa A.; Fujihira M.; Marti O. *Appl. Phys. Lett.*, 1997, 71, 2632-2634.
- [73] Mizes H. A.; Loh K. G.; Miller R. J. D.; Ahuja S. K.; Grabowski E. F. *Appl. Phys. Lett.*, 1991, 59, 2901-2903.
- [74] Radmacher M.; Tillmann R. W.; Gaub H. E. *Biophys. J.*, 1993, 64, 735-742.
- [75] Sugisaki K.; Nakagiri N.; Kinjo Y. *Langmuir*, 1999, 15, 5093-5097.
- [76] Troyon M.; Wang Z.; Pastre D.; Lei H. N.; Hazotte A. *Nanotechnology*, 1997, 8: 163-171.
- [77] Baek J.; Kim J. H.; Shin S.; Hong J. W.; Khim Z. G. *Jpn. J. Appl. Phys.*, 2006, 45, 2365-2367.
- [78] Hong J. W.; Kahng D. S.; Shin J. C.; Kim H. J.; Khim Z. G. *J. Vac. Sci. Technol. B*, 1998, 16, 2942-2946.
- [79] Hong J. W.; Kim B. I.; Kye J. I.; Khim Z. G. *J. Kor. Phys. Soc.*, 1997, 31: S83-87.
- [80] Shin S.; Baek J.; Hong J. W.; Khim Z. G. *J. Appl. Phys.*, 2004, 96, 4372-4377.
- [81] Burnham N. A. *Appl. Phys. Lett.*, 1993, 63, 114-116.
- [82] Palacio M. L. B.; Bhushan B. *Crit. Rev. Solid State Mater. Sci.*, 2010, 35, 73-104.
- [83] Dewulf, J.; Van Langenhove, H. Hydrocarbons in the atmosphere. In: Encyclopedia of Life Support Systems (EOLLS). Unesco: Paris, FR, 2003.
- [84] Rudolph, J.; Czuba, E.; Norman, A. L.; Huang, L.; Ernst, D. *Atmos. Environ.*, 2002, 36: 1173-1181.
- [85] Knapp, H. F.; Stemmer, A. *Surf. Interface Anal.*, 1999, 27, 324-331.
- [86] Kaupp, G.; Naimi-Jamal, M. R. *Scanning*, 2010, 32, 265-281.
- [87] Persson, B. N. J. Sliding Friction Physical Principles and Applications; second edition; Springer-Verlag: Berlin, DE, 2000.
- [88] Grandbois, M.; Beyer, M.; Rief, M.; Clausen-Schaumann, H.; Gaub, H. E. *Science*, 1999, 283, 1727-1730.
- [89] Pethica JB.; Oliver WC. 1987. Tip surface interaction in STM and AFM. *Phys. Scr. T*. 19, 61-66.
- [90] Hu, J.; Xiao, X. D.; Salmeron, M. *Appl. Phys. Lett.*, 1995, 67, 476-478.
- [91] Sarid, D. Scanning Force Microscopy: With Applications to Electric, Magnetic, and Atomic Forces, Oxford Univ. Press.: New York, NY, 1991.
- [92] Novotny V. J.; Karis T. E. *Appl. Phys. Lett.*, 1997, 71, 52-54.
- [93] Reprinted from *Ultramicroscopy*, 125, B. I. Kim and R. D. Boehm, Imaging Stability in Force-Feedback High-Speed Atomic Force Microscopy, 29-34, 2013, with permission from Elsevier.
- [94] Kim, B. I.; Clark, R.; Clark, T. *Scanning*, 2011, 33, 1-8.